

**Structure-rheology relationship in a sheared lamellar fluid**

S. J. Jaju and V. Kumaran

*Department of Chemical Engineering, Indian Institute of Science, Bangalore 560 012, India*

(Received 23 September 2015; published 22 March 2016)

The structure-rheology relationship in the shear alignment of a lamellar fluid is studied using a mesoscale model which provides access to the lamellar configurations and the rheology. Based on the equations and free energy functional, the complete set of dimensionless groups that characterize the system are the Reynolds number ( $\rho\dot{\gamma}L^2/\mu$ ), the Schmidt number ( $\mu/\rho D$ ), the Ericksen number ( $\mu\dot{\gamma}/B$ ), the interface sharpness parameter  $r$ , the ratio of the viscosities of the hydrophilic and hydrophobic parts  $\mu_r$ , and the ratio of the system size and layer spacing ( $L/\lambda$ ). Here,  $\rho$  and  $\mu$  are the fluid density and average viscosity,  $\dot{\gamma}$  is the applied strain rate,  $D$  is the coefficient of diffusion,  $B$  is the compression modulus,  $\mu_r$  is the maximum difference in the viscosity of the hydrophilic and hydrophobic parts divided by the average viscosity, and  $L$  is the system size in the cross-stream direction. The lattice Boltzmann method is used to solve the concentration and momentum equations for a two dimensional system of moderate size ( $L/\lambda = 32$ ) and for a low Reynolds number, and the other parameters are systematically varied to examine the qualitative features of the structure and viscosity evolution in different regimes. At low Schmidt numbers where mass diffusion is faster than momentum diffusion, there is fast local formation of randomly aligned domains with “grain boundaries,” which are rotated by the shear flow to align along the extensional axis as time increases. This configuration offers a high resistance to flow, and the layers do not align in the flow direction even after 1000 strain units, resulting in a viscosity higher than that for an aligned lamellar phase. At high Schmidt numbers where momentum diffusion is fast, the shear flow disrupts layers before they are fully formed by diffusion, and alignment takes place by the breakage and reformation of layers by shear, resulting in defects (edge dislocations) embedded in a background of nearly aligned layers. At high Ericksen number where the viscous forces are large compared to the restoring forces due to layer compression and bending, shear tends to homogenize the concentration field, and the viscosity decreases significantly. At very high Ericksen number, shear even disrupts the layering of the lamellar phase. At low Ericksen number, shear results in the formation of well aligned layers with edge dislocations. However, these edge dislocations take a long time to anneal; the relatively small misalignment due to the defects results in a large increase in viscosity due to high layer stiffness and due to shear localization, because the layers between defects get pinned and move as a plug with no shear. An increase in the viscosity contrast between the hydrophilic and hydrophobic parts does not alter the structural characteristics during alignment. However, there is a significant increase in the viscosity, due to pinning of the layers between defects, which results in a plug flow between defects and a localization of the shear to a part of the domain.

DOI: [10.1103/PhysRevE.93.032609](https://doi.org/10.1103/PhysRevE.93.032609)**I. INTRODUCTION**

Oil, water, and surfactants, when mixed in appropriate proportions, form structured fluids such as micellar, hexagonal, or lamellar mesophases. These are important in numerous commercial applications such as food and personal care products, and accurate prediction of the rheology of these structured fluids is of importance in the design of industrial processes. The lamellar mesophase, which consists of a stack of equally spaced layers at equilibrium is used in products where high viscosity is desired. Lamellar phases possess positional order in the direction perpendicular to the layers and fluidlike behavior along the plane of the layers. Intuitively, the shear flow is expected to align initially disordered lamellae along the flow direction, so as to form a well-aligned structure. The viscosity (defined as ratio of shear stress and strain rate) of the lamellar phase in this final configuration would then obey the inverse sum rule for viscosity of binary mixtures. In experiments, the steady state viscosity of a macroscopic sample is always orders of magnitude higher than that calculated by the inverse sum rule, indicating that there is significant disorder in the system [1–3]. There are, at present, no reliable models that can be used to predict the

macroscopic rheology, and the structure-rheology relationship, of disordered lamellar phases.

One reason for the difficulty of modeling lyotropic lamellar phases is the scale separation between the layer scale and typical sample sizes. The layer thickness is of the order of 1–10 nm, and a typical macroscopic sample of size 1 mm would contain about  $10^6$  layers. This scale separation also implies that a long time is required to achieve equilibrium, because the longest relaxation time diverges with system size [4]. In addition, due to the high viscosity of surfactant systems, the approach to equilibrium is slowed down by kinetic constraints at room temperature. The scale separation also makes it difficult to examine structure-property relations using simulations based on molecular models. The maximum system sizes that can be attained in molecular simulations is 1–2 bilayers, where the properties at the bilayer level such as the equilibrium spacing and the correlations in the height fluctuations can be studied, but not the collective properties of a stack of bilayers. At the mesoscale, continuum models, which do not resolve the molecular structure but only distinguish between the hydrophilic and hydrophobic parts of the lamellar fluid, can be used to simulate up to a few hundreds of layers. The other difficulty is the two-way structure-rheology relationship

in lamellar phases under large deformation. Not only are the rheological properties of lamellar fluids anisotropic, but the viscoelastic properties depend on the alignment of the layers relative to the principal axes of deformation, and the layer alignment is in turn modified by the flow [5,6]. It is necessary to include this two-way coupling between structure and flow in rheological models.

In the mesoscale description, the dynamical variable is the concentration (order-parameter) field which distinguishes the hydrophilic and hydrophobic parts. The free energy functional for the order parameter field is chosen to be a modification of the Landau-Ginzburg free energy which, when minimized, results in a periodic spatial variation in the concentration field with the correct lamellar spacing. Dynamical equations for the concentration and momentum fields, which are modifications of the model H equations [7] for a binary fluid, have been used to simulate the evolution of the structure and rheology of initially disordered lamellar samples [8–15]. These mesoscale models have been used in mesoscale simulations [11,13] to study the structure-rheology relationship for samples consisting of a few tens of layers. In these simulations, it is possible to identify defects in the background lamellar phase, visualize the annealing of defects due to shear, and also to identify the mechanisms of creation of defects due to the background shear. Two different defect creation mechanisms, the “buckling instability” (where defects are created due to expansion of layers along the extensional axis) and the “compressional instability” (where defects are created due to compression along the compressional axis) have been identified in the simulations. However, it should be noted that these studies are two dimensional, and it is not yet possible to simulate large system sizes consisting of even a few tens of layers in three dimensions.

The presence of defects in a background ordered lamellar phase could have a significant effect on the rheological properties. Experiments [16] show clear correlation between variations in viscosity and defect density. Simulations [8–15] have been used extensively to study restructuring of lamellar phases under shear. Simulation studies [13,14] also show that the layers align completely in small system sizes, and the viscosity value follows the inverse sum rule. Larger systems reach a steady state where there is a balance between annihilation and creation of defects, and the viscosity increases with system size. The defect creation mechanisms include the undulation instability along the extensional axis of layers subjected to an expansion, and compressional instability along the compressional axis of the shear flow [13]. Shear is also shown to reorganize ordered lamellar mesophases into multilamellar vesicles known as onion phases [17,18] by a mechanism that is still not well understood. It should be noted here that the largest system sizes in simulations, which comprise  $10^2$ – $10^3$  layers in two dimensions and a smaller number of layers in three dimensions, are still very small compared to macroscopic samples. Nevertheless, simulations do show that defects obstruct flow around them, modify resulting stresses and in turn could get created, deformed, or annealed due to the flow.

The common defect structures of relevance to lamellar phases are disclinations, edge dislocations, screw dislocations, and focal conic defects [19]. Focal conic defects arise because

the layers around a defect have to conform to shapes known as Dupin cyclides, in order to maintain the layer spacing constancy. Since focal conic defects typically involve hundreds of layers, they are visible in polarizing microscopy as fan-type structures. Additionally, self-assembled structures formed with defects as building blocks are finding potential applications in preparing lithographic templates, superhydrophobic surfaces, etc. [20]. Since the present study is restricted to two dimensions, not all defect structures are accessible. In two dimensions, there are two broad types of disorder that are observed [13]: edge dislocations in a background nearly aligned lamellar phase, and grain boundaries between two differently aligned domains. The edge dislocations in two dimensions are linked to the focal conic defects discussed above; the focal conic defects are formed when pairs of edge dislocations of opposite signs come together to form a dislocation pair (visible as long “oily streaks” in polarizing microscope images), and these break up perpendicular to the plane of the dislocation to form focal conics defects. Grain boundaries between different disordered domains are also visible in disordered lamellar mesophases in three dimensions [16], and the stability and dynamics of grain boundaries under shear has been studied [21]. The screw dislocation is the only defect type that is not present in two dimensions. Screw dislocations are known to have a significant effect on rheology in small amplitude strain measurements. However, a screw with an axis in any direction is not commensurate with continuous shearing, and so these are likely to be annealed quickly under steady shear.

Here, we identify a minimal set of dimensionless parameters which influence the rheology of the lamellar mesophase, and then we use continuum simulations in order to examine the effect of the variations in these parameters on the rheology during the shear alignment process from an initially disordered state in two dimensions. There are formal procedures to calculate the parameters in the mesoscale model from molecular properties [22,23], and it has been shown that the mesoscale model is able to capture linear response results of fundamental excitations of an aligned lamellar phase near equilibrium [22]. Theoretical approaches have also been developed for the effect of defects on the rheology of nearly aligned sheared lamellar mesophases [24]. However, there is as yet no comprehensive understanding of how the mesoscale parameters affect the rheology, and the structure-rheology relationship, for samples of size a few tens to hundreds of layers. For this, it is necessary to reduce the parameters in the problem to a minimal set of dimensionless groups, and then study the shear alignment as a function of these dimensionless parameters. Here, the effect of different dimensionless groups on the shear alignment process is studied for a modest system size of 32 layers in two dimensions. Even though the system size is not large, it is necessary to carry out a large number of simulations in order to sample variations in all the dimensionless parameters that are of importance, and to build a comprehensive picture of the different types of structures and the structure-rheology relationship.

The mesoscale free energy functional contains three parameters: the layer spacing  $\lambda$ , the energy density parameter  $A$ , and a parameter  $r$  which determines the thickness of the interface between the hydrophilic and hydrophobic parts. For

large  $r$ , the concentration modulation is sinusoidal, whereas for small  $r$ , the concentration modulation is close to a step function with a sharp transition between the hydrophilic and hydrophobic parts. There are three parameters in the dynamical concentration and momentum equations for the concentration field: the density, viscosity, and a diffusion coefficient or Onsager coefficient which is related to the permeability of the water through the bilayers. From these parameters, it is possible to construct three dimensionless numbers: the Reynolds number which is the ratio of fluid inertia and viscosity, the Schmidt number which is the ratio of momentum and mass diffusion, and the Ericksen number which is the ratio of the viscous and elastic stresses. In addition to these, there is also a possibility of a difference in viscosity between the hydrophobic and hydrophilic parts, because the hydrophilic component is usually water with relatively low viscosity, while the hydrophobic part contains surfactant tails which are long chain alkanes with relatively high viscosity. In the present analysis, we consider the Reynolds number to be small, because lamellar phases usually have very high viscosity. The effect of variations in the interface sharpness parameter  $r$ , the Schmidt number, the Ericksen number, and the viscosity contrast on the rheology during the shear ordering process are examined in detail. We have used single relaxation time lattice Boltzmann method (LBM), with two distribution functions, one each for concentration and momentum field, to perform the simulations [8,11,13]. The simulations have been carried out with wall [25] as well as periodic boundary conditions [26,27] for a system containing 32 lamellae in two dimensions.

## II. MODEL

The dimensionless scalar order parameter ( $\psi$ ) for concentration field is defined as the ratio of concentration difference of individual components ( $c_w - c_o$ ) and the total concentration ( $c_w + c_o$ ) where  $c_w$  and  $c_o$  are concentrations of hydrophilic (water) and hydrophobic (oil) parts. The lamellar mesophase is modeled using the model H mass and momentum equations for a binary fluid [7], with an additional term in the free energy functional which, when minimized, gives a one-dimensional periodically varying concentration field as the equilibrium solution [22,23]. Attention is restricted to symmetric lamellar phases where the hydrophilic and hydrophobic parts have equal volume fractions. A free energy functional can also be written for asymmetric systems where the volume fractions of the hydrophilic and hydrophobic parts are not equal, by adding a term that is cubic in the order parameter  $\psi$ , the coefficient of which is proportional to the relative difference in the volume fractions of the hydrophilic and hydrophobic parts [23]. However, we do not pursue this in the present analysis. The free energy functional ( $F[\psi]$ ) is of the form

$$F[\psi] = A \int dV \left( -\frac{1}{2}\psi^2 + \frac{1}{4}\psi^4 + \frac{g}{2k^2}(\nabla\psi)^2 + \frac{r}{2k^4}[(\nabla^2 + k^2)\psi]^2 \right). \quad (1)$$

The first two terms in the integral on the right are the quadratic and the quartic terms in the Landau-Ginzburg free energy

functional, and the negative sign on the first term promotes segregation of the constituent (hydrophilic and hydrophobic) parts. The third term is the surface tension term, and the value of parameter  $g$  is chosen so that the surface tension is zero at macroscale, as required by symmetry. The last term promotes formation of layers with wavelength (layer width)  $\lambda = (2\pi/k)$ , where  $k$  is the wave number. The parameter  $r$  in Eq. (1) controls the ratio of the wavelength of the concentration modulation and the thickness of the interface over which there is a transition between the hydrophilic and hydrophobic regions, as discussed a little later.

At macroscale, the free energy functional is written in terms of layer displacement variable  $u$  which is the local displacement of the layers from their equilibrium positions due to applied stresses. The free energy functional for the displacement field, derived from that for the concentration field (1) using the linearization approximation, is [22]

$$F[u] = \int dV \left\{ \frac{B}{2} \left( \frac{\partial u}{\partial y} \right)^2 + \frac{G}{2} \left[ \left( \frac{\partial u}{\partial x} \right)^2 + \left( \frac{\partial u}{\partial z} \right)^2 \right] + \frac{K}{2} \left( \frac{\partial^2 u}{\partial x^2} + \frac{\partial^2 u}{\partial z^2} \right)^2 \right\}. \quad (2)$$

The first term in the integrand represents the free energy change due to compression or expansion of layers along the layer normal, and  $B$  is the compression modulus. The second term accounts for the change in free energy due to the change in area in the plane of the layers, and  $G$  is the surface tension. Since the free energy of the lamellar mesophase system is invariant when the layers are tilted, the surface tension  $G$  is zero. The third term is the energy penalty due to layer bending, and  $K$  is the bending (curvature) modulus. For a single membrane, the free energy is written as an integration over the membrane area, such that

$$F[u] = \int ds \left\{ \frac{B^*}{2} \left( \frac{\partial u}{\partial y} \right)^2 + \frac{G^*}{2} \left[ \left( \frac{\partial u}{\partial x} \right)^2 + \left( \frac{\partial u}{\partial z} \right)^2 \right] + \frac{K^*}{2} \left( \frac{\partial^2 u}{\partial x^2} + \frac{\partial^2 u}{\partial z^2} \right)^2 \right\}, \quad (3)$$

where  $ds$  is the differential surface area of the membrane. It is easy to see that  $B = B^*/\lambda$ ,  $G = G^*/\lambda$ , and  $K = K^*/\lambda$ . The relation between the free energy functional (1) for the concentration field, and that in Eq. (2) for the displacement field, is shown in Appendix A. Also provided are the mass and momentum equations expressed in terms of the concentration and the displacement fields. The simulation technique, based on the lattice Boltzmann method (LBM), is described in Appendix B.

Based on the description in Appendix A, the dimensionless parameters which influence the equilibrium and dynamical properties are as follows:

(1) The Schmidt number ( $Sc = \nu/D$ ) is defined as the ratio of momentum diffusivity and mass diffusivity. Here,  $D$  is the diffusion coefficient for the concentration field  $\psi$ , and is related to the permeation coefficient for water through the hydrophobic regions of the bilayer as shown in Appendix A. The kinematic viscosity  $\nu$  is the ratio of the dynamic viscosity  $\mu$  and the density  $\rho$ ,  $\nu = (\mu/\rho)$ . The Schmidt number is varied from 0.33 to 5.0 in the most of the simulations, though we have

considered lower values of the Schmidt number in some cases to distinguish qualitatively different morphologies during the alignment process.

(2) The interface parameter  $r$  determines the thickness of the interface between the hydrophilic and hydrophobic parts in the lamellar mesophase. Once  $r$  is fixed, the parameter  $g$  is determined from the requirement that the surface tension has to be zero [Eq. (A7)]. The equilibrium interface profiles for three values of  $r$  shown in Fig. 28 in Appendix A. It was shown [22,23] that the molecular concentration profiles from molecular simulations can be used to construct the concentration field  $\psi$ , and this can be used to evaluate the parameter  $r$  which can then be used in mesoscopic simulations. For large  $r$ , the concentration profile resembles a sinusoidal profile. This corresponds to the weak segregation or high temperature limit where there is interdiffusion of the hydrophobic and hydrophilic parts and the layers are weakly defined. For small  $r$ , the concentration profile resembles a step function. This is the strong segregation limit where the hydrophilic and hydrophobic parts do not diffuse through each other.

Simulations have been carried out for three different values of  $r$ : 1.0, 0.1, and 0.01 (cases 1, 6, and 7 in Table I). For  $r = (1, 0.1, 0.01)$  the value of interface thickness ( $r^{1/4}\lambda$ ) is ( $\lambda, 0.56\lambda, 0.32\lambda$ ) respectively.

(3) In the dynamical equations, the ratio of the inertial and viscous forces is the Reynolds number ( $\text{Re} = \rho \bar{\gamma} L^2 / \bar{\mu}$ ), where  $\bar{\gamma}$  is the average strain rate and  $\bar{\mu}$  is the average viscosity. Though the Reynolds number is usually defined in terms of the flow velocity, it is more convenient to define it in terms of the strain rate which is the ratio of the difference in the velocities of the two walls (or periodic images when Lees-Edwards boundary conditions are used) and the separation  $L$ . The Reynolds number is usually low in practical applications, and so we set it to a value of 1 in the simulations which is low enough that inertial effects are not important.

(4) The dimensionless Ericksen number ( $\text{Er}$ ) is defined as the ratio of viscous stress to the elastic stress due to nonequilibrium structure. Here, we prefer a definition based on layer compression modulus which has dimensions of energy per unit volume, so that the Ericksen number is independent of the system size,

$$\text{Er} = \frac{\bar{\mu} \bar{\gamma}}{B}, \quad (4)$$

where we have used average strain rate instead of flow velocity to define the Ericksen number. When the compression modulus  $B$  is used, the Ericksen number is independent of the system size.

To examine the effect of Ericksen number on the shear alignment, simulations are also carried out for four other values, namely 0.49 (case 3), 4.9 (case 2), 0.1 (case 4), and  $4.9 \times 10^{-3}$  (case 5), in addition to the reference value of 0.2.

(5) The effect of viscosity variation across one wavelength of the concentration modulation is incorporated using a model for the viscosity of the form

$$\mu = \text{Maximum}[\mu_0[1 + \mu_1\psi(\mathbf{x}, t)], 0.01\mu_0], \quad (5)$$

where  $\psi(\mathbf{x}, t)$  is the local concentration. Four different values of  $\mu_1$  are considered, 0.32, 0.53, 1.07, and 2.13, for a diffuse

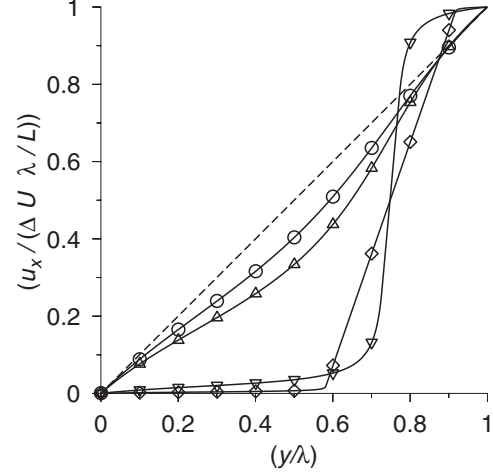


FIG. 1. The mean velocity  $u_x$ , scaled by the difference in velocity across one concentration modulation,  $(\Delta U \lambda / L)$ , as a function of the cross-stream distance  $(y/\lambda)$  for an aligned lamellar phase with viscosity contrast with the parameter  $\mu_1 = 0.32$  ( $\circ$ ), 0.53 ( $\Delta$ ), 1.07 ( $\nabla$ ), and 2.13 ( $\diamond$ ) in Eq. (5). The dashed line shows the linear velocity profile when there is no viscosity contrast,  $\mu_1 = 0$ .

interface with  $r = 1$ . For the last two values, in order to prevent the viscosity from becoming negative, a condition is imposed on the minimum value for the viscosity, as indicated in Eq. (5). The velocity profiles across one concentration wave,  $\psi = \sin(2\pi y/\lambda)$ , when the viscosity is given by Eq. (5) is shown in Fig. 1. For  $\mu_1 = 0.32$  and 0.53, there is only a small modification in the velocity profile from the linear profile for  $\mu_1 = 0$ . In contrast, for  $\mu_1 = 1.07$  and 2.13, shear banding is clearly observed where there is a near-linear variation of velocity across the region with low viscosity and virtually no change in the velocity in the regions with high viscosity, as expected for a water-surfactant lyotropic lamellar mesophase.

While the median viscosity is  $\mu_0$  when the viscosity variation is given by Eq. (5), the average viscosity (stress divided by the ratio of the velocity difference across one concentration wave and the wavelength) is given by the inverse sum rule,

$$\bar{\mu} = \left( \frac{1}{\lambda} \int_0^\lambda dy \frac{1}{\mu(y)} \right)^{-1}. \quad (6)$$

This average viscosity could be much smaller than the median viscosity when  $\mu_1$  is greater than 1, as shown in Table II. The viscosity ratio is defined as the ratio of the difference between the maximum and minimum viscosities and the average viscosity. This ratio is also numerically large when  $\mu_1$  is greater than 1. In the following analysis, the Reynolds, Schmidt, and Ericksen numbers, denoted by  $\text{Re}_0$ ,  $\text{Sc}_0$ , and  $\text{Er}_0$ , are defined on the basis of the viscosity  $\mu_0$ , and not the viscosity  $\bar{\mu}$ . The ratios of the Reynolds, Schmidt, and Ericksen numbers defined using  $\mu_0$  and  $\bar{\mu}$  are given in Table II. The details of the implementation of viscosity contrast in the simulations are given in Appendix B.

(6) Periodic boundary conditions are used in the simulations along the flow ( $x$ ) direction. In the direction perpendicular to the flow, two different types of boundary conditions are used: the no-slip boundary condition (where the fluid velocity is set

equal to the wall velocity and the value of the concentrations is set equal to zero) [25], and the Lees-Edwards boundary [26,27] conditions, where periodic images of the simulation cell above and below are moved with velocity  $(\dot{\gamma}L/2)$  and  $-(\dot{\gamma}L/2)$  respectively, in order to create a shear flow with strain rate  $\dot{\gamma}$  within the simulation cell. Here,  $\dot{\gamma}$  is the applied strain rate and  $L$  is the height of the box. The implementation of these two types of boundary conditions is discussed in Appendix B. The no-slip boundary conditions are implemented using the bounce-back scheme of Ladd [25], while the constant concentration condition ensures that there is no change in the concentration at the boundary after the streaming and collision time steps [13]. The boundary conditions are briefly explained in Appendix B. These two types of simulations do not show any qualitative differences and quantitative differences are not significant, so we present results only for the wall boundary conditions here. A comparison between the results obtained with the two boundary conditions is shown in Fig. 31 in Appendix B.

Table I in Appendix A contains a comprehensive list of the dimensionless parameters in the simulations. For cases with viscosity contrast, the viscosity used in the dimensionless parameters can be either  $\mu_0$  [Eq. (5)], which is the median viscosity, or the average viscosity for a layered configuration calculated using the inverse sum rule. In the present analysis, the viscosity  $\mu_0$  is used for all the dimensionless parameters. The relation between the average viscosity  $\bar{\mu}$  and  $\mu_0$ , as well as the values of dimensionless parameters determined using  $\bar{\mu}$ , are provided in Table II in Appendix A.

The initial disordered configuration is generated using a uniform random number generator. For systems with relatively smoother interfaces ( $r \geq 0.1$ ), the initial value of  $\psi$  at each lattice site is set to a value  $\pm 0.5$  depending upon the outcome of the random number generator. When the same protocol was used for initialization of systems with steep interface, regions of high concentration gradients at length scales smaller than the layer spacing were found to exist even at much later time in simulations ( $>500\dot{\gamma}t$ , where  $\dot{\gamma}$  is the strain rate). To avoid formation of such domains, and to generate an initial concentration profile with smaller gradients, a different initialization protocol is used. In this case, the system is divided into number of blocks of equal size. Each block is assigned a value of  $\pm 1$  randomly (with equal probability), as opposed to a lattice site in the previous protocol. The concentration ( $\psi$ ) field value at a particular lattice site inside a block is a weighted fraction of the value assigned to the block. The weights are decided as follows: Each block is further divided into concentric spherical shells. All the lattice sites within a shell are assigned an equal weight inversely proportional to the radius of the spherical shell. The concentration field then varies gradually within each block and the outer most lattice sites in each block have nearly same values (close to zero) ensuring a smooth interface between neighboring blocks. A contour plot of these blocks could be seen in Figs. 18(b) and 18(d).

Different measures are examined in order to quantify the extent of order in the system, and the relationship between the ordering and rheology.

(1) The layer configurations and concentration fields are examined visually to classify the different types of ordering

that take place. In the images of the layer configurations, the hydrophobic ( $\psi < 0$ ) and hydrophilic ( $\psi > 0$ ) regions are distinguished using two colors and the lines represent contours of  $\psi = 0$ ; the resolution in the figures is not sufficient to plot the details of the concentration fields over the entire domains. In order to examine the concentration variations, contour plots of the concentration field over smaller domains are shown separately.

(2) The root mean square of the concentration fluctuations, defined as

$$\langle \psi^2 \rangle = \frac{1}{V} \int dV \psi(\mathbf{x})^2, \quad (7)$$

is useful for identifying the degree of homogenization in the lamellar mesophase system. For sinusoidal concentration profile ( $r = 1$ , diffuse interface), the root mean squared ( $\sqrt{\langle \psi^2 \rangle_0}$ ) value of concentration fluctuations is 0.81. Hence during simulations, if  $\sqrt{\langle \psi^2 \rangle}$  approaches 0.81, it implies locally phases are well segregated; while a value smaller than 0.81 implies incomplete segregation between the hydrophilic and hydrophobic parts. The  $\sqrt{\langle \psi^2 \rangle_0}$  value for  $r = 0.1$  and 0.01 is 0.85 and 0.88 respectively.

(3) The total free energy ( $F[\psi]$ ) attains a minimum at equilibrium when the layers are completely aligned, and disorder leads to an increase in  $F[\psi]$ . Hence,  $F[\psi]$  could be used as an order parameter to monitor the alignment process.

(4) In large systems, we expect disorder to be primarily in the form of defects in a background ordered lamellar phase. Due to the disorder in the concentration field at defect locations, the gradient terms in free energy would be larger than the quadratic and quartic contributions in the free energy functional. Hence we define an order parameter ( $f$ ), which considers only the increase in energy due to gradients as follows:

$$f = \frac{1}{V} \int dV [(\nabla^2 + k^2)\psi]^2. \quad (8)$$

The parameter  $f$  is isotropic; it is zero if the layer spacing is  $2\pi/k$ , irrespective of the layer orientation.

(5) We define a new order parameter,  $f_{\hat{\mathbf{n}}}$ , in order to ascertain the orientation of the formed layers as follows:

$$f_{\hat{\mathbf{n}}} = \frac{1}{V} \int dV [(\hat{\mathbf{n}} \cdot \nabla)^2 + k^2]\psi^2, \quad (9)$$

where  $\hat{\mathbf{n}}$  is a unit vector. As mentioned earlier, in the present study, the shear flow is simulated by moving the bottom bounding surface (mirror images when the Lees-Edwards boundary condition is used) towards the right (positive  $x$  direction) and the top surface in the opposite direction. To determine whether the layers are aligned along the flow direction due to applied shear we set  $\hat{\mathbf{n}} = \mathbf{e}_y$  (unit vector along the  $y$  direction) and the corresponding orientation order parameter then is

$$f_y = \frac{1}{V} \int dV [(\partial_y^2 + k^2)\psi]^2. \quad (10)$$

The parameter  $f_y$  is sensitive to gradients in concentration field only along the shear direction and would be equal to zero if the system is perfectly aligned with normal along the shear direction.

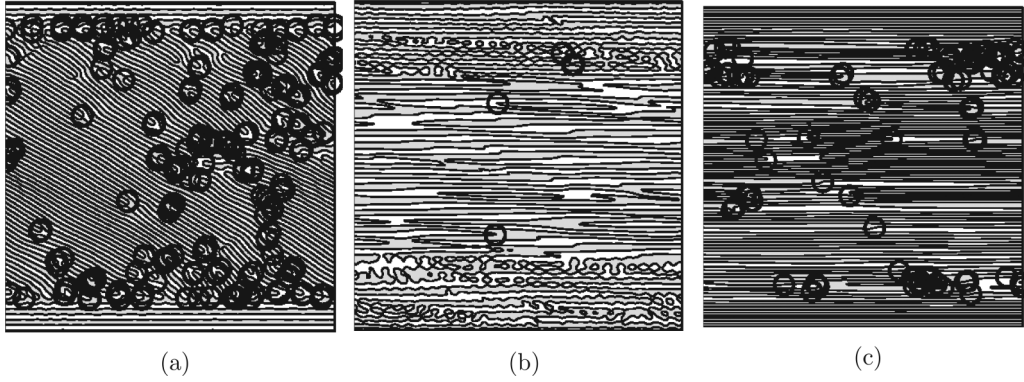


FIG. 2. Defects identified using Eq. (11) shown in black circles for three different parameter values:  $Sc_0 = 0.33$ ,  $Er_0 = 0.2$ ,  $r = 1$ ,  $\dot{\gamma}t = 87$  (a);  $Sc_0 = 1$ ,  $Er_0 = 4.9$ ,  $r = 1$ ,  $\dot{\gamma}t = 27$  (b); and  $Sc_0 = 5$ ,  $Er_0 = 0.2$ ,  $r = 0.01$ ,  $\dot{\gamma}t = 257$  (c). The defect locations are correctly predicted in case (a). In other cases, they are sometimes overpredicted for steep interfaces for  $r < 1$  (c) or underpredicted because the concentration field is not equilibrated locally for high  $Er$  (b). The lines show contours of zero concentration.

(6) To understand the relation between structure and dynamics, it is necessary to identify the defects in the system and relate their behavior with parameters based on rheology. A site is characterized as a defect based on two criteria. First all the possible defect sites are identified by comparing the value of local defect energy  $d(\mathbf{x})$ , defined as

$$d(\mathbf{x}) = \frac{Ar}{2k^4} [(\nabla^2 + k^2)\psi]^2. \quad (11)$$

A location is identified as part of a defect if  $d(\mathbf{x})$  is larger than a cutoff, and the cutoff is set using the procedure explained in Ref. [13]. In a system with uniform concentration [ $\psi(\mathbf{x}) = \psi_0$ ], the local defect energy  $d_0$  would be equal to  $(Ar\psi_0^2/2)$  everywhere. We use a suitable fraction (0.1) of this value as defect energy cutoff ( $d_{\text{cutoff}} = 0.1d_0$ ). At the defect core, an edge dislocation is at least  $(\lambda/2)$  units in width. Thus, there should be  $(\lambda/2)$  lattice sites which would exceed the local defect energy cutoff, and a defect is identified only if the number of defect sites is greater than  $(\lambda/2)$  in both directions. The defect density then is the number of defect sites per unit area. This procedure works fairly accurately in identifying edge dislocations in an otherwise well-aligned lamellar background, as shown in Figs. 2(a) and 25 when the concentration profile is sinusoidal ( $r = 1$ ) and the layers are well formed. They are usually overpredicted for low values of  $r$  when the interfaces are sharp, as shown in Fig. 2(c), and are underpredicted at high Ericksen number, as shown in Fig. 2(b). The defects observed in our simulations are edge

dislocations, which are defined by their ‘‘Burgers vector.’’ The Burgers vector is defined as the vector from the start to the end of the Burgers loop, over a contour moving anti-clockwise as shown in Fig. 3. For the present two-dimensional simulations, where there are defects in a background well-aligned lamellar phase with layers along the  $x$  direction, the magnitude of the Burgers vector is 2 since there is one incomplete layer in between nearly aligned layers, and the Burgers vector is directed along either the  $+y$  or  $-y$  direction, as shown in Fig. 3. Isolated edge dislocations cannot disappear in the bulk since they are topological defects, and it is necessary for dislocations of opposite sign to come together and cancel for the system to anneal.

(7) In linear shear flow, the local flow velocity  $u_x(\mathbf{x})$  is given by the relation  $\dot{\gamma}y$ , where  $\dot{\gamma}$  is the strain rate and  $y$  is the distance from the zero velocity stream line in the cross stream direction. The presence of disorder in the structure (concentration field) however modifies the local velocity field. To quantify this deviation, we define velocity field order parameter ( $\langle \Delta \dot{\gamma}^2 \rangle$ ) as

$$\langle \Delta \dot{\gamma}^2 \rangle = \frac{1}{V(\dot{\gamma}L)^2} \int dV (u_x(\mathbf{x}) - \dot{\gamma}y)^2. \quad (12)$$

The parameter  $\langle \Delta \dot{\gamma}^2 \rangle$  will be zero in the case of linear shear flow with no viscosity contrast. When there is viscosity contrast,  $\dot{\gamma}$  will be a function of the order parameter ( $\psi$ ), and so  $\langle \Delta \dot{\gamma}^2 \rangle$  will be nonzero even for the perfectly aligned lamellar

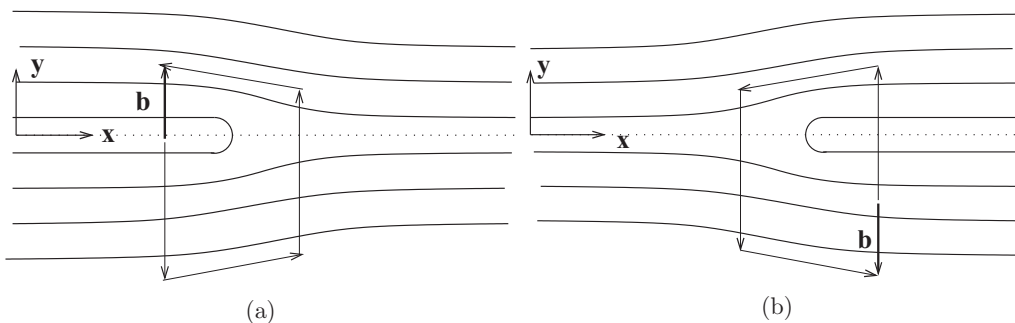


FIG. 3. Edge dislocation with Burgers vector in the  $+y$  direction (a) and  $-y$  direction (b).

phase. For systems with a nonzero value of  $(\Delta\mu/\bar{\mu})$  chosen in this study, the value of  $\langle\Delta\dot{\gamma}^2\rangle$  in the perfectly aligned state, calculated using simulations, is 0.0061, 0.0116, 0.1267, and 0.1274, respectively, for  $\mu_1 = 0.32, 0.53, 1.07,$  and  $2.13$  in Eq. (5).

(8) In a perfectly aligned state the fluid viscosity is equal to bare fluid viscosity ( $\bar{\mu}$ ). However, under imposed flow, the divergence of the stress tensor in Eq. (A12) has an additional contribution proportional to  $(\frac{\delta F}{\delta \psi})$ . The macroscopic fluid viscosity (defined as the ratio of shear stress and applied strain rate) then would be higher than that in the aligned state ( $\bar{\mu}$ ). The scaled shear viscosity ( $\mu$ ) is defined as the ratio of average viscosity (stress across the configuration divided by the strain rate, which is the ratio of the velocity difference and the distance between the top and bottom surfaces) ( $\mu'$ ) and  $\bar{\mu}$ , i.e.,

$$\mu = \frac{\mu'}{\bar{\mu}}. \quad (13)$$

For the perfectly aligned system,  $\mu = 1$ .

Simulations have been carried out for at least three different randomly generated initial configurations in each case, and the mean and standard deviations are determined by averaging over the three different runs. The error bars in the simulations show one standard deviation above and below the mean value. In the graphs, the points and error bars are shown only at representative location values, to enhance clarity.

### III. RESULTS AND ANALYSIS

The simulations, based on the lattice Boltzmann method (LBM), have been carried out at different values of parameters shown in Table I for a two dimensional (2D) system of size  $32\lambda \times 32\lambda$ , where  $\lambda$  is the wavelength of the concentration modulation. In cases 1–5, variations in the Schmidt and Ericksen number are considered (Sec. III A) for a diffuse interface with  $r = 1$  and no viscosity contrast. Cases 6 and 7 involve a variation in the interface thickness (Sec. III B) for  $Er_0 = 0.2$ , no viscosity contrast, and a range of Schmidt numbers. The viscosity contrast between the hydrophilic and hydrophobic parts of the bilayer is varied in cases 8–11 (Sec. III C) for a diffuse interface with  $r = 1$ ,  $Er_0 = 0.2$ . It should be noted that the dimensionless numbers are all defined using the constant  $\mu_0$  in Eq. (5); the conversion between dimensionless numbers based on  $\mu_0$  and  $\bar{\mu}$  is given in Table II.

#### A. Schmidt and Ericksen numbers

We first examine how variations in the Schmidt number affect the shear alignment for a smooth interface ( $r = 1$ ) and constant viscosity [ $\mu_1 = 0$  in Eq. (5)] [13], in order to provide a reference for the effect of interface thickness, relative viscosity, and Ericksen number on the rheology. Figure 4 shows  $\psi$  evolution with time for different values of the Schmidt number. For  $Sc = 0.33$ , we see the formation of domains of layers with different orientations at intermediate time [see concentration field configuration at  $\dot{\gamma}t = 5$  in Fig. 4(a)]. The domains with layers along the extensional axis grow at the expense of other domains as time progresses [ $\dot{\gamma}t = 20$ – $50$  in Fig. 4(a)]. Bilayer deformation and movement leads to alignment along

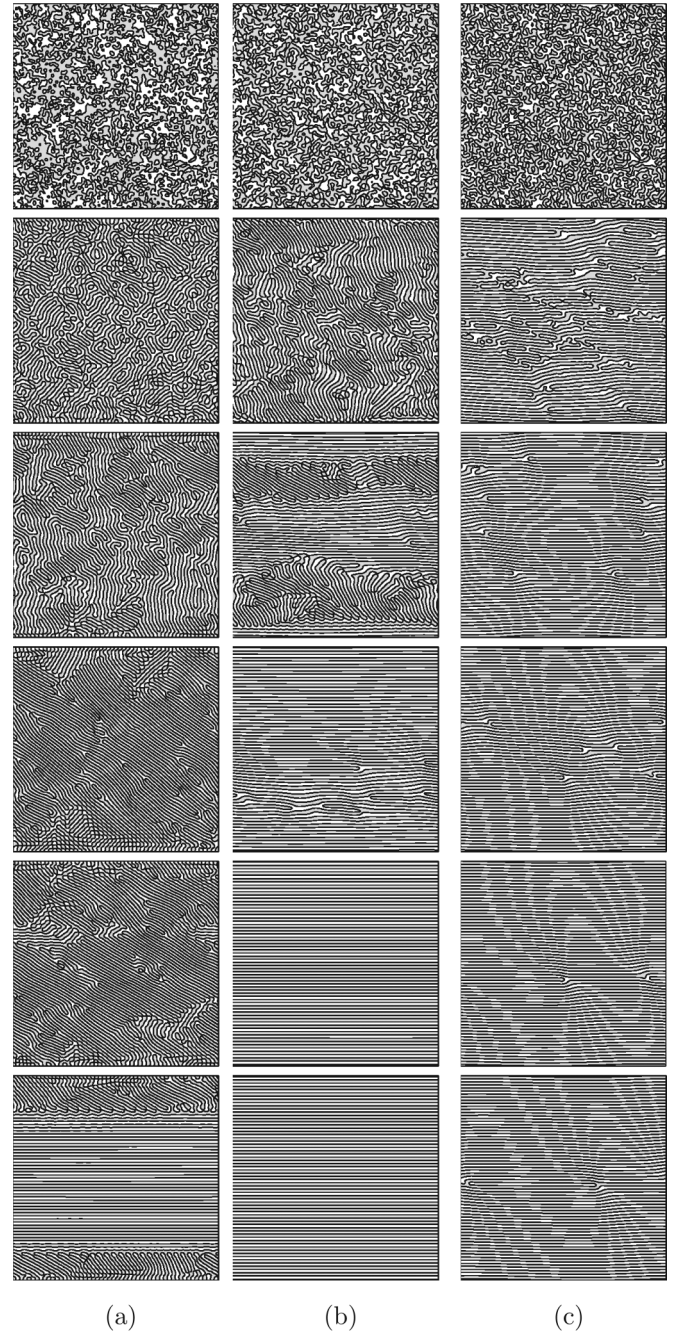


FIG. 4. Layer evolution for  $Sc_0 = 0.33$  (a),  $Sc_0 = 1.0$  (b), and  $Sc_0 = 5.0$  (c) for  $r = 1$ , and  $Er_0 = 0.2$  at (from top to bottom)  $\dot{\gamma}t = 0.1, 5, 20, 50, 100, 350$ . The lines show contours of zero concentration.

the flow, though distinct domains continue to exist even at later times ( $\dot{\gamma}t = 100$ ). The appearance of shear banding, that is of aligned and misaligned domains forming bands in the gradient direction, is observed in the long time limit for  $\dot{\gamma}t > 100$ , leading to ordering at very long times. In most cases, the layers in the bands are aligned in one of two directions, either in the flow direction or along the extensional axis. The domains with alignment along the extensional axis shrink while those with alignment along the flow direction grow, leading to ordering at long times. The qualitative behavior can also be inferred

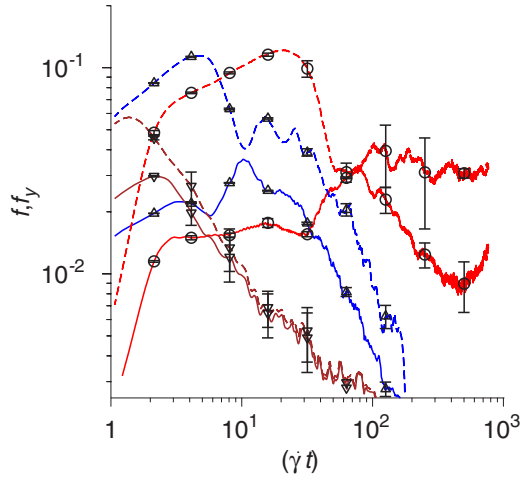


FIG. 5. The variation of  $f$  (solid line) and  $f_y$  (dashed line) with scaled time ( $\dot{\gamma}t$ ) for an initially disordered lamellar mesophase at  $Er_0 = 0.2$ ,  $r = 1$ , and  $Sc_0 = 0.33$  (red,  $\circ$ ),  $Sc_0 = 1.0$  (blue,  $\Delta$ ) and  $Sc_0 = 5.0$  (brown,  $\nabla$ ).

from the behavior of the order parameters  $f$  and  $f_y$  with time, shown in Fig. 5, where it is observed that  $f_y$  is significantly greater than  $f$  for  $Sc = 0.33$ , implying that the concentration field relaxes locally to a sinusoidal profile but the layers do not align along the flow direction. At  $Sc_0 = 0.33$ , mass diffusion is faster than momentum diffusion, and so the concentration field equilibrates fast locally, but the local domains are not aligned with the global direction of least resistance to flow. For  $Sc = 5$ , where momentum diffusion is faster than mass diffusion, alignment takes place due to breakage of misaligned layers and reformation of layers aligned along the flow, as shown in Fig. 4(c). The layers are aligned in the flow direction even before they are fully formed [compare the  $\psi$  field at  $\dot{\gamma}t = 5$  in Fig. 4(c) with corresponding field in Fig. 4(a)]. As time progresses, these partially formed layers join together and form an aligned configuration that spans the domain. This can be seen from later ( $\dot{\gamma}t = 20$ – $350$ ) configurations of concentration field in Fig. 4(c). Consequently, parameters  $f$  and  $f_y$  quickly become equal for  $Sc_0 = 5$ , as shown in Fig. 5, and then decrease due to ordering. However, there are still edge dislocations in the background well-aligned system.

We now analyze the shear alignment process of systems at  $Sc_0 = 1$ , where the mass and momentum diffusivities have equal magnitudes. Based on the concentration field evolution shown in Fig. 4(b), we see that the alignment mechanism for systems at  $Sc_0 = 1$  is morphologically similar to that for the system with  $Sc_0 = 0.33$  at early times ( $\dot{\gamma}t < 5$ ), and to  $Sc_0 = 5$  at later times ( $\dot{\gamma}t > 20$ ), and then there is complete alignment for  $\dot{\gamma}t > 100$ . As can be seen from comparison of Figs. 4(a)–4(c), the time taken for shear alignment appears to have a minimum for  $Sc_0 = 1$ . This is because the shear banding seen in the long time limit for  $Sc_0 = 0.33$  appears at shorter times for  $Sc_0 = 1$ , and this results in a localization of the edge defects which then efficiently cancel. An analysis of parameters  $f$  and  $f_y$  with time for  $Sc_0 = 1$  (Fig. 5) confirms the presence of misaligned domains at short times, and the existence of defects in a background lamellar phase at long times.

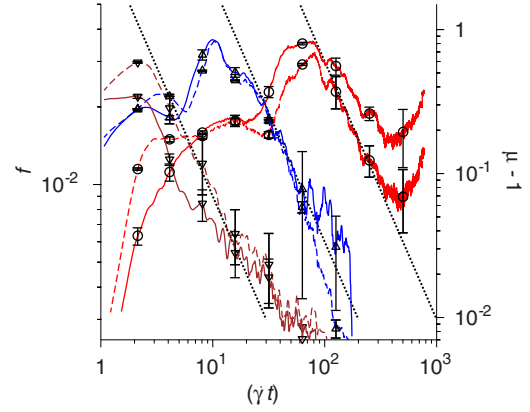


FIG. 6. The variation of  $\mu - 1$  (solid line, right y axis) and  $f$  (dashed line, left y axis) with time for an initially disordered lamellar mesophase at  $Er_0 = 0.2$ ,  $r = 1$ , and  $Sc_0 = 0.33$  (red,  $\circ$ ),  $Sc_0 = 1.0$  (blue,  $\Delta$ ), and  $Sc_0 = 5.0$  (brown,  $\nabla$ ). The dotted lines indicate a slope of  $-1$  on the log-log graphs.

Although not shown here, the concentration field evolution for  $Sc_0 = 0.66$  and  $Sc_0 = 2$  are morphologically similar to that for  $Sc_0 = 0.33$  and  $Sc_0 = 5$  respectively. From this, we conclude that at lower Schmidt numbers ( $Sc_0 \leq 1$ ), alignment takes place due to initial rotation of microdomains formed due to local relaxation of concentration field, followed by growth of domains aligned along the extensional axis at the expense of layers aligned along the compressional axis, and later growth of layers aligned along the flow direction and shrinkage of layers aligned along the extensional axis. At higher Schmidt numbers ( $Sc_0 > 1$ ), alignment of layers along the flow direction is due to melting and reformation of layers, resulting in a well aligned system with edge dislocations, which have to approach each other and cancel for complete alignment. However, unlike the  $Sc_0 = 0.33$  case, the  $f$  and  $f_y$  values tend to zero in the long time limit for  $Sc_0 = 0.66$  and  $2$ , implying that the system aligns completely.

The relationship between the order parameter  $f$  and the viscosity is examined in Fig. 6, where the parameter  $f$  is plotted on the left y axis and the difference between the scaled viscosity and the bare viscosity of an ordered lamellar phase, ( $\mu - 1$ ), is plotted on the right y axis. It is evident that there is a strong correlation between  $f$  and  $\mu - 1$ . For high Schmidt number ( $Sc_0 > 1$ ), both  $f$  and ( $\mu - 1$ ) initially increase, reach a maximum, and then decrease in time. The time required to reach the maximum values of  $f$  and  $\mu - 1$  decreases as the Schmidt number is increased. The system takes longer to reach the maximum viscosity and  $f$  for  $Sc_0 = 0.33$ , and both  $f$  and ( $\mu - 1$ ) do not decrease to zero even for the largest ( $\dot{\gamma}t$ ) in the simulations, since the system does not reach the fully ordered state. The maximum value of the viscosity decreases as the Schmidt number is increased due to the difference in the mechanism of alignment—the nearly aligned background lamellar phase with defects, observed at high Schmidt number, has a lower viscosity than the intermediate state with domains containing layers aligned along the extensional direction at low Schmidt number. The relationship between defect density and viscosity is examined in Fig. 7. The defect density also increases with time under steady shear, reaches a maximum,

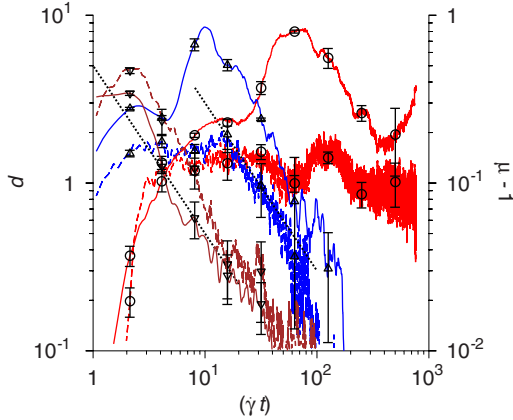


FIG. 7. The time variation of the defect density  $d$  (dashed line, right y axis) and  $\mu - 1$  (solid line, left y axis) at  $Er_0 = 0.2$ ,  $r = 1$ , and  $Sc_0 = 0.33$  (red,  $\circ$ ),  $Sc_0 = 1.0$  (blue,  $\Delta$ ), and  $Sc_0 = 5.0$  (brown,  $\nabla$ ). The dotted lines indicate a slope of  $-1$  on the log-log graphs.

and then decreases in a manner similar to  $f$  and the viscosity for  $Sc_0 \geq 1$ . However, the maximum of the defect density increases as the Schmidt number is increased, in contrast to the viscosity. This is because at high Schmidt number, the incompletely formed layers give rise to a larger number of defects in comparison to the misaligned domains at low Schmidt numbers. At  $Sc_0 = 0.33$ , the defect density first increases as the layers form, but does not decrease upon further shearing, in contrast to the viscosity. The defect density exhibits much larger fluctuations in time; we have tried other criteria for identifying defects, and the best results are those reported in Fig. 7. Thus, despite the ease of visually identifying defect locations, it is difficult to define a quantitative criterion which does not exhibit large fluctuations. The defect numbers also do not correspond very well to the viscosity, and the parameter  $f$  appears to be a much better structural indicator of the rheology of the system at  $Er_0 = 0.2$ .

A salient feature of the time variation of structural parameters and viscosity is the decrease proportional to  $(\dot{\gamma}t)^{-1}$  as time increases. This characteristic is clearly evident over a decade of variation in  $\dot{\gamma}t$  in Fig. 6 for all Schmidt numbers, and is evident to a lesser extent in the defect density in Fig. 7. This variation of defect density and viscosity proportional to  $t^{-1}$  is expected if the alignment takes place due to the cancellation of defects of opposite signs due to shear [24]. This mechanism is expected at high Schmidt numbers where the structure at intermediate time consists of nearly aligned layers distorted by the presence of edge dislocations, in which defects of opposite sign cancel when they approach each other due to shear. However, in the simulations, the  $f$  and the viscosity decrease proportional to  $t^{-1}$  even at  $Sc_0 = 0.33$ .

In simulations so far, the Ericksen number  $Er_0 = (\mu_0\dot{\gamma}/B)$ , is set to 0.2. Since the Reynolds number and the system size ( $L$ ) are kept constant during the simulations, a variation in Ericksen number would also change the compression modulus ( $B$ ) and the bending modulus ( $K$ ) of lamellae, and the energy density  $A$  in the equation for the free energy functional [Eq. (1)]. The shear alignment process has also been examined for two higher values of Ericksen numbers, 0.49 and 4.9. The configurations

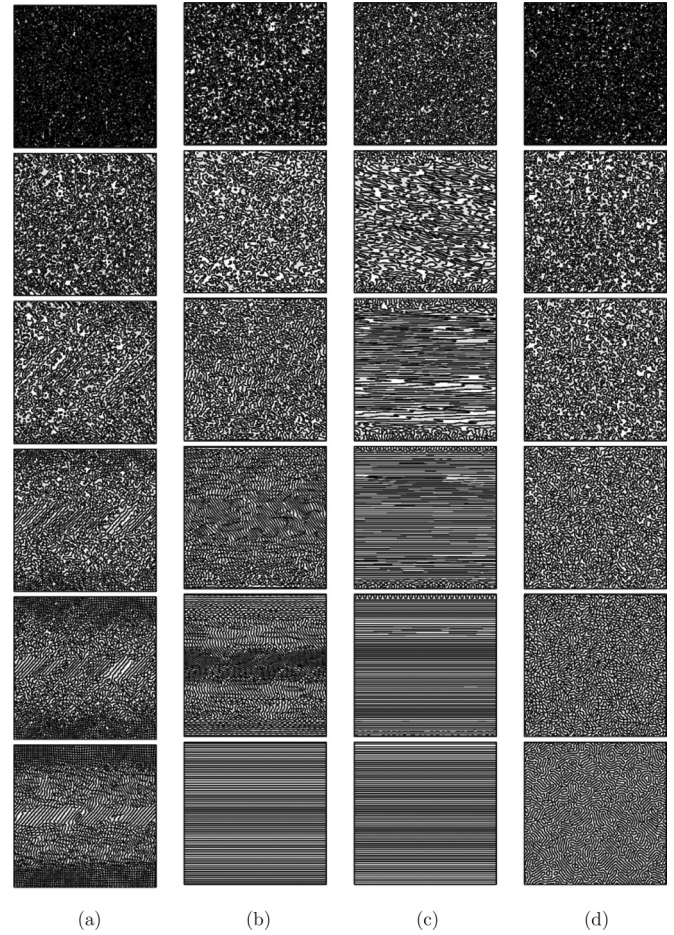


FIG. 8. Layer evolution for  $Sc_0 = 0.2$  (a),  $Sc_0 = 0.33$  (b), and  $Sc_0 = 5.0$  (c), and the layer evolution without shear at  $Sc_0 = 0.2$  (d) at  $Er_0 = 4.9$  and  $r = 1$  at (top to bottom)  $\dot{\gamma}t$  [equivalent lattice time steps for (d)] = 0.1, 5, 20, 50, 100, 350. The lines show contours of zero concentration.

are shown in Fig. 8 for  $Er_0 = 4.9$  at ( $Sc_0 = 0.2, 0.33$ , and 5). The qualitative features of the ordering at  $Er_0 = 0.49$  and 4.9 are similar to that at  $Er_0 = 0.2$ . At low Schmidt number, there is the formation of domains with layers aligned along the extensional axis at intermediate times [Fig. 8(b)]. At high Schmidt number, alignment takes place by the breakage and reformation of layers, as shown in Fig. 8(c). However, the transition between the two different types of ordering occurs at a lower Schmidt number (between 0.2 and 0.33) in comparison to that for  $Er_0 = 0.2$ . There are also significant differences. At low Schmidt number  $Sc_0 = 0.2$  close to the boundaries, there is breakage of layers, and the formation of what appear to be vesicles through an apparent pearling instability even in the long time limit [Fig. 8(a)] at  $\dot{\gamma}t \geq 100$ . Such instability is not observed when the initially disordered system is allowed to evolve without shear [see Fig. 8(d)]. At  $Er_0 = 4.9$ , the layers are not as sharply defined as that at  $Er_0 = 0.2$  during the shear ordering process. This is shown by the gray-scale contour plots of the concentration field in Fig. 9. For low Ericksen number, there is large variation in the concentration even at early times, but as the Ericksen number increases, the concentration is close to 0 throughout the domain, indicating

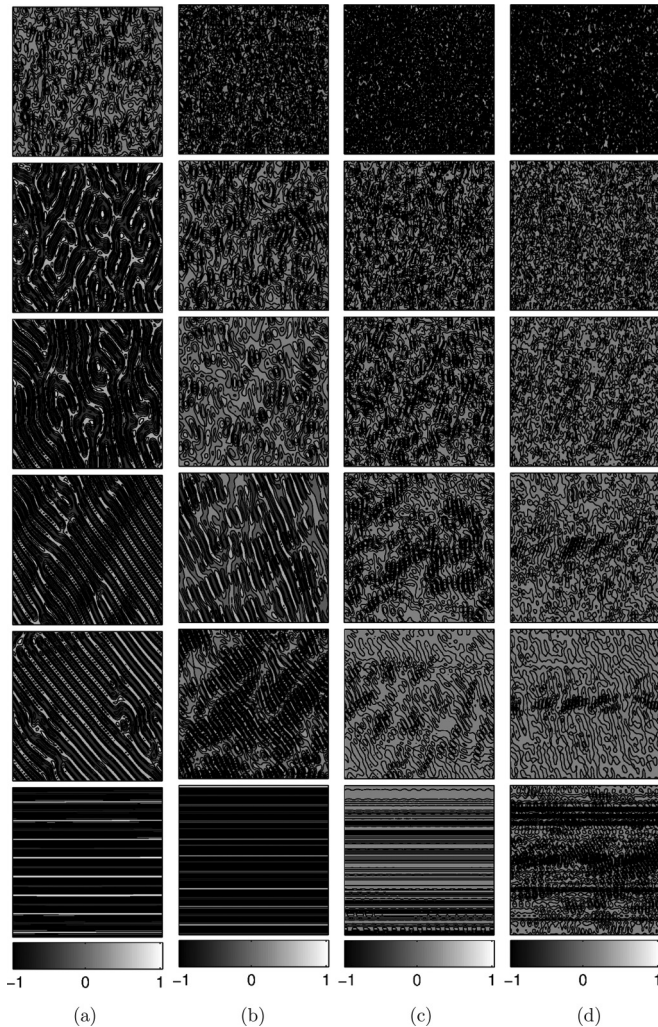


FIG. 9. Contour plots of concentration field evolution for  $Er_0 = 0.2$  (a), 4.9 (b), 49 (c), and 490 (d) at  $Sc_0 = 0.33$  at, from top to bottom,  $\dot{\gamma}t = 0.1, 5, 20, 50, 100, 350$  respectively. Only the central  $8\lambda \times 8\lambda$  portion is shown for clarity.

that separation of the hydrophilic and hydrophobic constituents in the lamellar phase is suppressed due to shear. This is because the viscous stresses are much larger than the elastic stress, and the viscous stresses prevent the layers from attaining their equilibrium configurations. This indicates that there may be an upper limit on the shear rate (or Ericksen number) beyond which a well-defined lamellar phase cannot be formed.

The structural order parameter  $f$  for  $Er_0 = 0.49$  and  $4.9$  are shown in Fig. 10. At high Schmidt number, it takes longer for  $f$  to reach its maximum values as the Ericksen number increases, but there is also a rapid decrease in  $f$  as the system quickly reaches the well aligned state after the peak in the disorder. At low Schmidt number ( $Sc_0 = 0.33$ ), there is significant disorder even in the long time limit for  $Er_0 = 0.49$ , though the disorder decreases for  $Er_0 = 4.9$ . At the lowest Schmidt number of  $0.2$  for  $Er_0 = 4.9$ , both  $f$  (and  $f_y$ , not shown here for conciseness) increase with time due to the significant disorder generated by the breakage of layers at boundaries and the pearling instability; the system never reaches a well-aligned state in this

case. The correlation between structure and viscosity is shown in Fig. 10. Here,  $\mu - 1$ , the difference between the apparent viscosity and the viscosity of an aligned sample, is shown along with the order parameter  $f$ . The magnitude of  $\mu - 1$  decreases significantly as the Ericksen number is increased, in contrast to the disorder parameter  $f$  which increases as the Ericksen number is increased. This indicates that even though there is an increase in the disorder with an increase in the Ericksen number, the disordered domains offer lower resistance to flow. There is a good correlation between  $f$  and the viscosity for  $Er_0 = 0.49$ , though the correlation is poor for  $Er_0 = 4.9$ . At high Schmidt number  $Sc_0 = 5$ , the  $(\mu - 1) \propto t^{-1}$  scaling for the viscosity is evident even at  $Er_0 = 4.9$ . At intermediate Schmidt number,  $Sc_0 = 1.0$  for  $Er_0 = 0.49$  and  $Sc_0 = 1.0$  and  $0.33$  for  $Er_0 = 4.9$ , the viscosity first increases and then decreases sharply when the system orders to the perfectly aligned state. At low Schmidt number,  $Sc_0 = 0.33$  for  $Er_0 = 0.49$  and  $Sc_0 = 0.2$  for  $Er_0 = 4.9$ , the viscosity does not decrease to zero even after a thousand strain units, but seems to attain a steady state in which there is significant disorder.

The evolution of the root mean square of the concentration field,  $\langle \psi^2 \rangle$  averaged over the entire domain [Eq. (7)], provides further insight into the reason for the decrease in the viscosity despite the increase in the disorder (as reflected by the parameters  $f$  and  $f_y$ ) as the Ericksen number is increased. As shown in Fig. 11, the root mean square of the concentration fluctuations quickly reaches its equilibrium value when the Ericksen number is  $0.2$  or lower, but there is a considerable delay in attaining the equilibrium value at high Ericksen number. In particular, at  $Er_0 = 0.2$ , the root mean square of the concentration is close to its steady-state value within about 5 strain units [see  $\psi$  field snapshot at  $\dot{\gamma}t = 5$  in Fig. 9(a)]; in contrast at  $Er_0 = 4.9$ , it takes more than 100 strain units for the  $\sqrt{\langle \psi^2 \rangle}$  to reach the steady state value (compare  $\psi$  fields at  $\dot{\gamma}t = 100$  at different  $Er_0$  in Fig. 9). Interestingly, at  $Er_0 = 4.9$ , the value of  $\sqrt{\langle \psi^2 \rangle}$  first decreases up to about 10 strain units, and then increases, indicating that shear initially tends to mix and homogenize the disordered state. This can be seen at  $\dot{\gamma}t = 50$  in Fig. 9. The application of a shear flow disrupts the segregation of the hydrophilic and hydrophobic parts; increasing Ericksen number enhances mixing (see  $\psi$  fields in Fig. 9). The concentration homogeneity due to the delay in segregation results in a very low viscosity combined with high disorder parameters  $f$  and  $f_y$ . After about 100 strain units, the concentration modulation is aligned perpendicular to the flow direction at  $Er_0 = 4.9$ , and then the segregation proceeds until the root mean square of the concentration fluctuations attains its final steady state value [see snapshot at  $\dot{\gamma}t = 350$  in Fig. 9(b)]. At  $Er_0 = 490$ , the concentration does not reach its equilibrium value even after 1000 strain units, and the value of  $\sqrt{\langle \psi^2 \rangle}$  is one to two orders of magnitude smaller than the equilibrium value.

The evolution of the concentration field at a low value of Ericksen number,  $Er_0 = 4.9 \times 10^{-3}$ , is shown in Fig. 12. In this case, the layers are very sharply defined even at the very early times. The two distinct types of ordering, which are the formation of disordered domains with grain boundaries at low Schmidt numbers and the presence of defects in a well-aligned background at high Schmidt number, are observed in

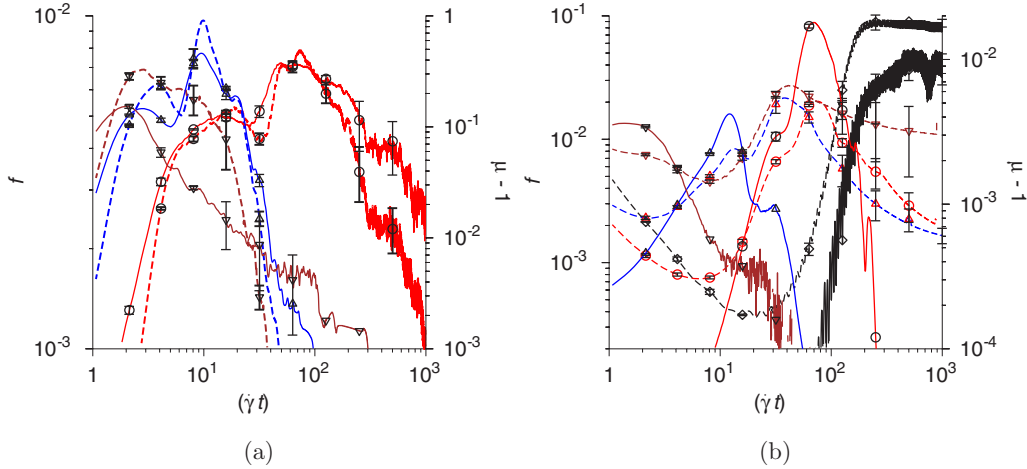


FIG. 10. The variation of  $f$  (dashed line, left y axis) and  $\mu - 1$  (solid line, right y axis) with scaled time  $(\dot{\gamma}t)$  for an initially disordered lamellar mesophase at  $r = 1$ ,  $Er_0 = 0.49$  (a) and  $Er_0 = 4.9$  (b), and  $Sc_0 = 0.33$  (red,  $\circ$ ),  $Sc_0 = 1.0$  (blue,  $\Delta$ ),  $Sc_0 = 5.0$  (brown,  $\nabla$ ), and only for (b),  $Sc_0 = 0.2$  (black,  $\diamond$ ).

this case as well. However, there is a significant shrinkage of misaligned domains at intermediate times at low Schmidt number, resulting in the formation of well aligned layers with edge dislocations. The evolution of the configuration at  $Er_0 = 0.1$  is similar to that at  $Er_0 = 0.2$  [compare  $\psi$  fields in Figs. 4(a) and 12(a) at  $Sc_0 = 0.33$  and 4(c) and 12(b) at  $Sc_0 = 5.0$ ]. There is however, a rather dramatic change in the evolution of the structural order parameters as the Ericksen number is decreased from 0.1 to  $4.9 \times 10^{-3}$ , as shown in Fig. 14. At  $Er_0 = 0.1$ , the parameters  $f$  and  $f_y$  do not decrease to zero for  $Sc_0 = 0.33$  where there are persistent defects in the long time limit (see Fig. 6 for the equivalent evolution for  $Er_0 = 0.2$ ), but they do decrease to zero in the long time limit for higher values of the Schmidt number. There is a difference between  $f$  and  $f_y$  at low Schmidt numbers due to the formation of disordered domains with grain boundaries, but there is less difference at high Schmidt number due to the presence of defects in a background aligned lamellar phase. For the lowest value

of  $Er_0 = 4.9 \times 10^{-3}$ , the system does not completely align even after 300 strain units, and there is a persistent difference between  $f$  and  $f_y$  at all times. This result is surprising because the layer configurations in Figs. 12(c) and 12(d) indicate the presence of defects in a background of well aligned layers, and the reason for the difference is the following. Since the layers are very stiff at low Ericksen numbers, defects result in a significant tilt of layers which persists for long distances. Due to the long-range tilt generated by defects,  $f_y$  is significantly higher than  $f$  even though there are relatively few defects in a well-aligned background, as shown in Fig. 13. The stiffness of the layers also prevents the breakage and reformation of layers which is required for the glide of defects in the cross-stream direction and the annihilation of defects. Due to this, the time taken for complete ordering increases as the Ericksen number decreases. However, the variation in the parameters  $f$  and  $f_y$  at  $Er_0 = 0.1$  is similar to that for  $Er_0 = 0.2$ , as shown in Fig. 13. In contrast, for  $Er_0 = 4.9 \times 10^{-3}$ , there is a

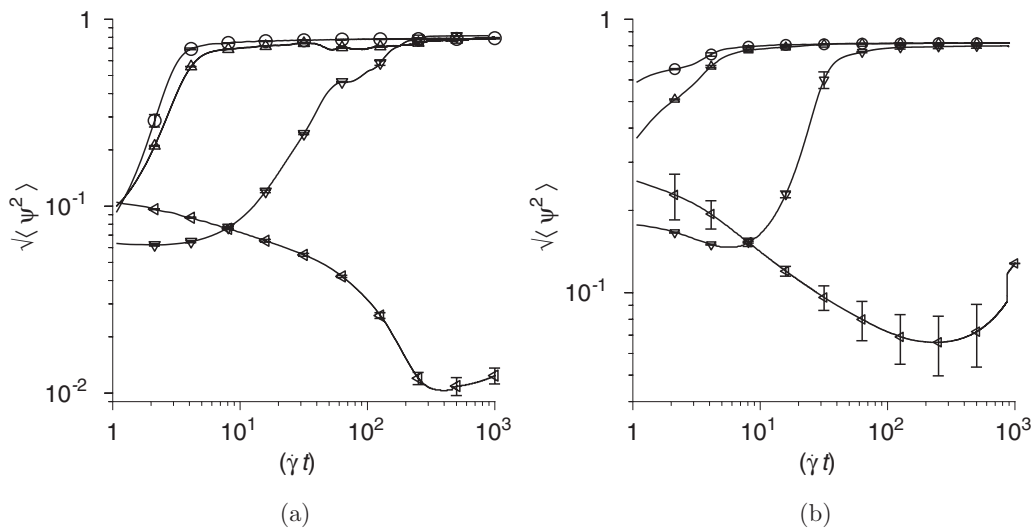


FIG. 11. The variation of the root mean square of the concentration averaged over the entire domain,  $\sqrt{\langle \psi^2 \rangle}$ , with  $\dot{\gamma}t$  for  $Er_0 = 0.2$  ( $\circ$ ),  $0.49$  ( $\Delta$ ),  $4.9$  ( $\nabla$ ), and  $490$  ( $\triangleleft$ ) for  $r = 1$ , for  $Sc_0 = 0.33$  (a) and  $Sc_0 = 5.0$  (b).

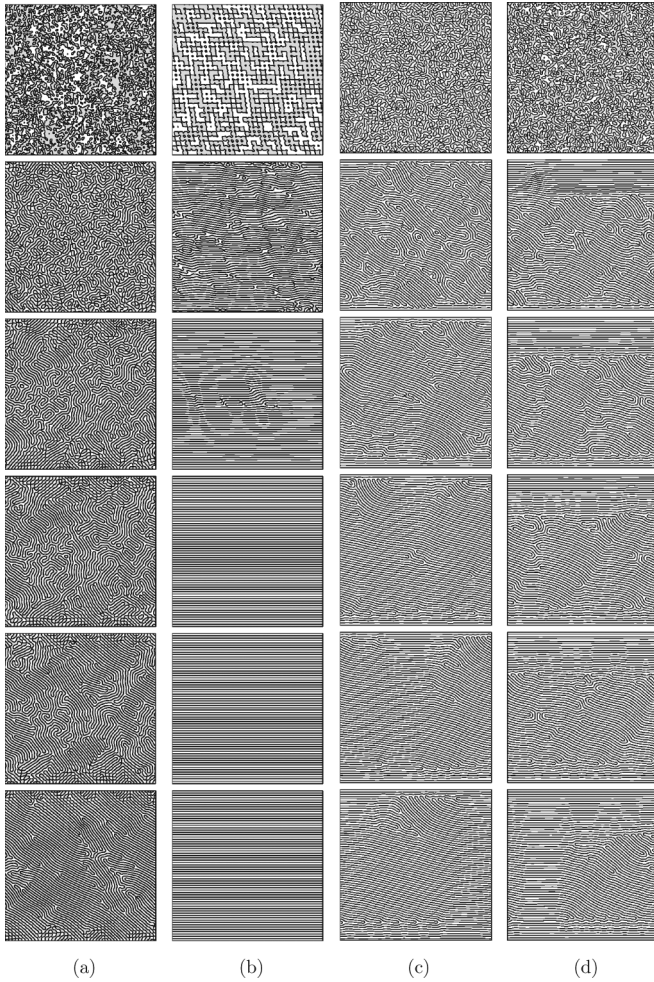


FIG. 12. Layer evolution at  $Er_0 = 0.1$ , (a) and (b), and  $4.9 \times 10^{-3}$ , (c) and (d), for  $Sc_0 = 0.33$ , (a) and (c), and 5, (b) and (d). Top to bottom,  $(\dot{\gamma}t) = 0.1, 5, 20, 50, 100, 350$ . The lines show contours of zero concentration.

decrease in  $f$  and  $f_y$  in the long time limit even at low Schmidt numbers.

The stiffness of the layers also results in a significantly higher viscosity at  $Er_0 = 4.9 \times 10^{-3}$ , as compared to that at  $Er_0 = 0.1$ , as shown in Fig. 14. At  $Er_0 = 0.1$ , the scaled viscosity does not decrease to 1 in the long time limit only at low Schmidt number  $Sc_0 = 0.33$ , and shows a decrease proportional to  $t^{-1}$  for high Schmidt number. For  $Er_0 = 4.9 \times 10^{-3}$ , the scaled viscosity is significantly larger, and it does not decrease to 1 even after 400 strain units for any value of the Schmidt number. Even though the structural order parameter  $f$  is smaller by an order of magnitude, the viscosity is higher by an order of magnitude for  $Er_0 = 4.9 \times 10^{-3}$  in comparison to  $Er_0 = 0.1$ . This is because the small number of edge dislocations at low Ericksen number, and the consequent layer tilt which seems to span the system, results in a significantly higher resistance to flow. At  $Er_0 = 4.9 \times 10^{-3}$ , the viscosity does decrease as the Schmidt number is increased, though the correlation between the structural order parameter and viscosity is not as good as that at higher Ericksen number. The significant increase in viscosity at  $Er_0 = 4.9 \times 10^{-3}$  is

due to the rigidification of the layers between defects or the defect pinning mechanism, as shown in Fig. 15. Even though the layer configurations contain a relatively small number of defects, as shown in Figs. 15(a)–15(c), there is no straining in the region between the defects, and the strain is localized to the near-wall regions, as shown in the velocity profiles in Fig. 15(d). Due to this strain localization and shear banding, the apparent viscosity is much higher than the fluid viscosity. In contrast, at  $Er_0 = 0.2$ , there is straining throughout the system as shown in Fig. 16(d), despite the disorder in the configurations shown in Figs. 16(a)–16(c). Since the velocity profiles are nearly linear, the apparent viscosity is close to the true fluid viscosity.

The shear localization at high Ericksen number is illustrated in Fig. 17, which shows the parameter  $\langle \Delta \dot{\gamma}^2 \rangle$  [Eq. (12)] which provides a measure of the departure of the velocity profile from the linear velocity profile. The value of  $\langle \Delta \dot{\gamma}^2 \rangle$  at  $Er_0 = 4.9 \times 10^{-3}$  is higher by an order of magnitude in comparison to that at  $Er_0 = 0.1$  at low and high Schmidt numbers. The qualitative nature of the variation of  $\langle \Delta \dot{\gamma}^2 \rangle$  is also independent of the Schmidt number at  $Er_0 = 4.9 \times 10^{-3}$ . At high Schmidt number, the value of  $\langle \Delta \dot{\gamma}^2 \rangle$  remains large even after 300 strain units for  $Er_0 = 4.9 \times 10^{-3}$ , in contrast to the behavior at high Ericksen number where  $\langle \Delta \dot{\gamma}^2 \rangle$  decreases when the system reaches a well aligned state.

## B. Interface thickness

The evolution of concentration field ( $\psi$ ) for systems with a thin interface ( $r < 1$ ) are shown in Fig. 18. At  $Sc_0 = 0.33$ , [Figs. 18(a) and 18(b)], the evolution of the  $\psi$  field is qualitatively similar to that for diffuse interfaces  $r = 1$ , exhibiting the formation of misaligned domains at  $\dot{\gamma}t = 5$ , and the deformation of these domains due to shear from  $(\dot{\gamma}t = 20)$  onward. Although concentration field contours at intermediate Schmidt numbers ( $Sc_0 = 0.6$ –2) and  $r < 1$  are not shown, the shear alignment mechanism for systems with  $Sc_0 \leq 1$  is qualitatively similar. The evolution in  $\psi$  field with time for  $Sc_0 = 5$  and  $r < 1$  is shown in Figs. 18(c) and 18(d). The alignment process for  $Sc_0 = 5$  exhibits the melting and reformation mechanism seen in shear alignment of systems with smooth interfaces (Fig. 4). However, there are significant variations in layer thickness during reformation (see the concentration field for  $\dot{\gamma}t = 20$ –50). Figures 18(c) and 18(d) show that the layers are aligned in the long time limit at  $\dot{\gamma}t = 350$ , but there are still variations in the layer thickness.

The order parameters  $f$  and  $f_y$  are shown as a function of dimensionless time for  $r = 0.1$  and  $r = 0.01$  in Fig. 19. The magnitude of the order parameters becomes larger as  $r$  decreases, as evidenced by comparing Fig. 5 (for  $r = 1$ ) and Fig. 19. This is primarily due to the variability in the layer spacing when the interfaces are sharp, as seen in Fig. 18. Unlike the case of a diffuse interface with  $r = 1$  (Fig. 5), the values of parameters  $f$  and  $f_y$  in Fig. 19 for  $Sc_0 = 1$  and 5 do not decrease to zero in the long time limit even after hundreds of units of strain. This is because the concentration field and the layer spacing have not equilibrated, and the wavelength of concentration modulation is different from the wavelength that

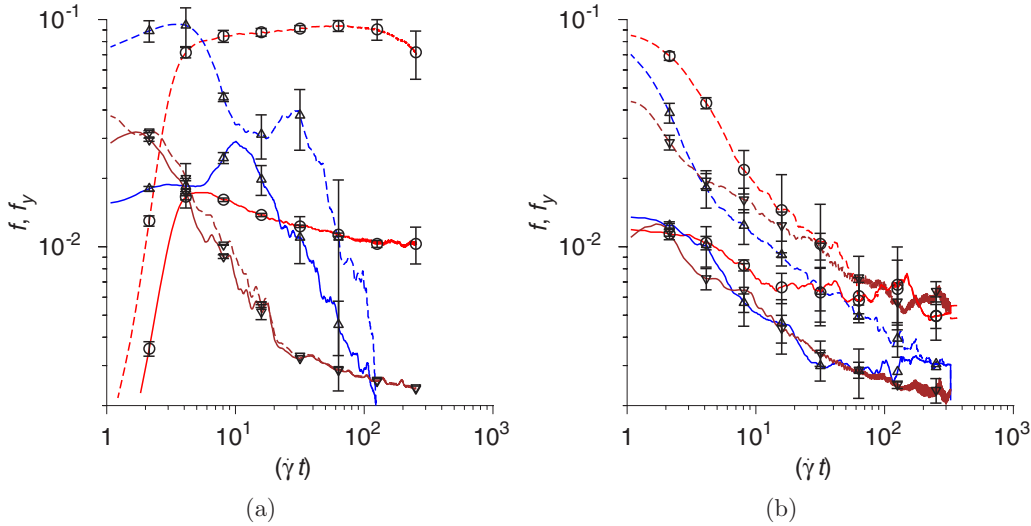


FIG. 13. The variation of  $f$  (solid line) and  $f_y$  (dashed line) with scaled time  $(\dot{\gamma}t)$  for an initially disordered lamellar mesophase at  $r = 1$ ,  $Er_0 = 0.1$  (a), and  $Er_0 = 4.9 \times 10^{-3}$  (b), and  $Sc_0 = 0.33$  (red,  $\circ$ ),  $Sc_0 = 1.0$  (blue,  $\Delta$ ),  $Sc_0 = 5.0$  (brown,  $\nabla$ ).

minimizes the free energy functional ( $F[\psi]$ ). Accordingly, in Fig. 18, we see lamellae with varying thickness even at  $\dot{\gamma}t = 350$ . The difference between  $f$  and  $f_y$  is evident even at long times for  $Sc = 0.33$ , because the layer normals are not aligned in the gradient direction even after hundreds of strain units. However, for  $Sc = 1.0$  and  $5.0$ , both  $f$  and  $f_y$  are equal at long times, indicating that the layer normals are perpendicular to the flow direction, even though the layer spacing has not attained equilibrium.

Though there is an increase in the parameters  $f$  and  $f_y$  as  $r$  decreases due to the imperfect development of the concentration profile, the viscosity decreases as  $r$  decreases, as shown in Fig. 20. There is a poor correlation between the viscosity and the parameters  $f$  and  $f_y$  in Fig. 19, but there is a very good correlation between the viscosity increase and the departure from linearity of the velocity field, as shown in Fig. 20. For given Schmidt number, the value of  $\langle \Delta \dot{\gamma}^2 \rangle$  [Eq. (12)] is much smaller for steep interfaces ( $r = 0.01, 0.1$ )

than for smooth interfaces ( $r = 1$ ). Thus, despite the very high disorder in the system, the velocity profile is nearly linear and the effective viscosity, even for a highly disordered state, is low. Figure 20 also shows that there is a rather sharp decrease in the scaled excess viscosity  $(\mu - 1)$  when the system aligns between 200 and 100 strain units for  $Sc_0 = 1$  and  $5$  respectively, due to the formation of layers that are aligned but which have not yet attained their equilibrium spacing. However, the decrease in  $\mu - 1$  proportional to  $t^{-1}$  is apparent for  $Sc_0 = 5$  at long times, and to a lesser extent for  $Sc_0 = 1$  at intermediate times. For  $Sc_0 = 0.33$ , the system does not reach an aligned state even for strain units of the order of 300, and the scaled viscosity is significantly higher than 1.

Even though the shear alignment at low  $r$  shares many of the features of that at high Ericksen number, including low viscosity and high disorder parameters  $f$  and  $f_y$ , the low viscosity here is not due to imperfect segregation between the hydrophilic and hydrophobic parts (as was the case at high

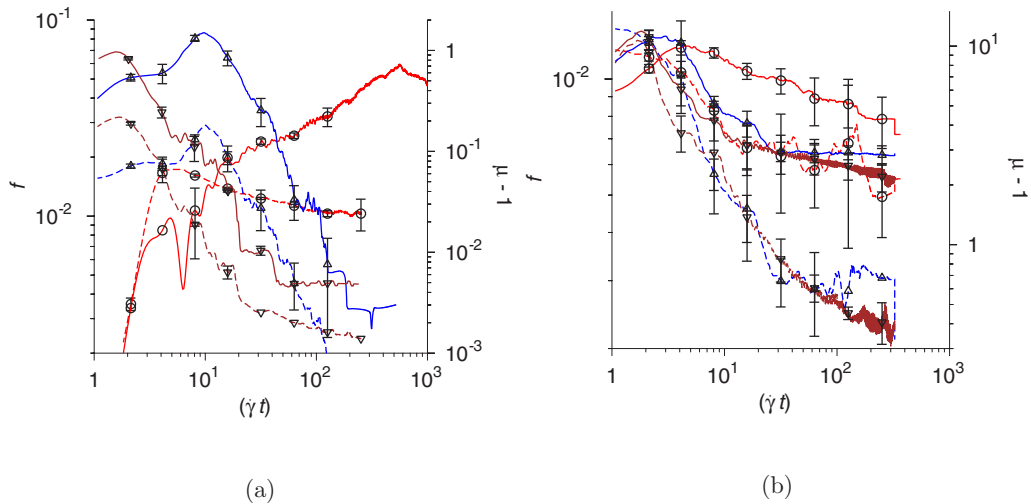


FIG. 14. The variation of  $f$  (dashed line, left y axis) and  $\mu - 1$  (solid line, right y axis) with scaled time  $(\dot{\gamma}t)$  for an initially disordered lamellar mesophase at  $r = 1$ ,  $Er_0 = 0.1$  (a) and  $Er_0 = 4.9 \times 10^{-3}$  (b), and  $Sc_0 = 0.33$  (red,  $\circ$ ),  $Sc_0 = 1.0$  (blue,  $\Delta$ ),  $Sc_0 = 5.0$  (brown,  $\nabla$ ).

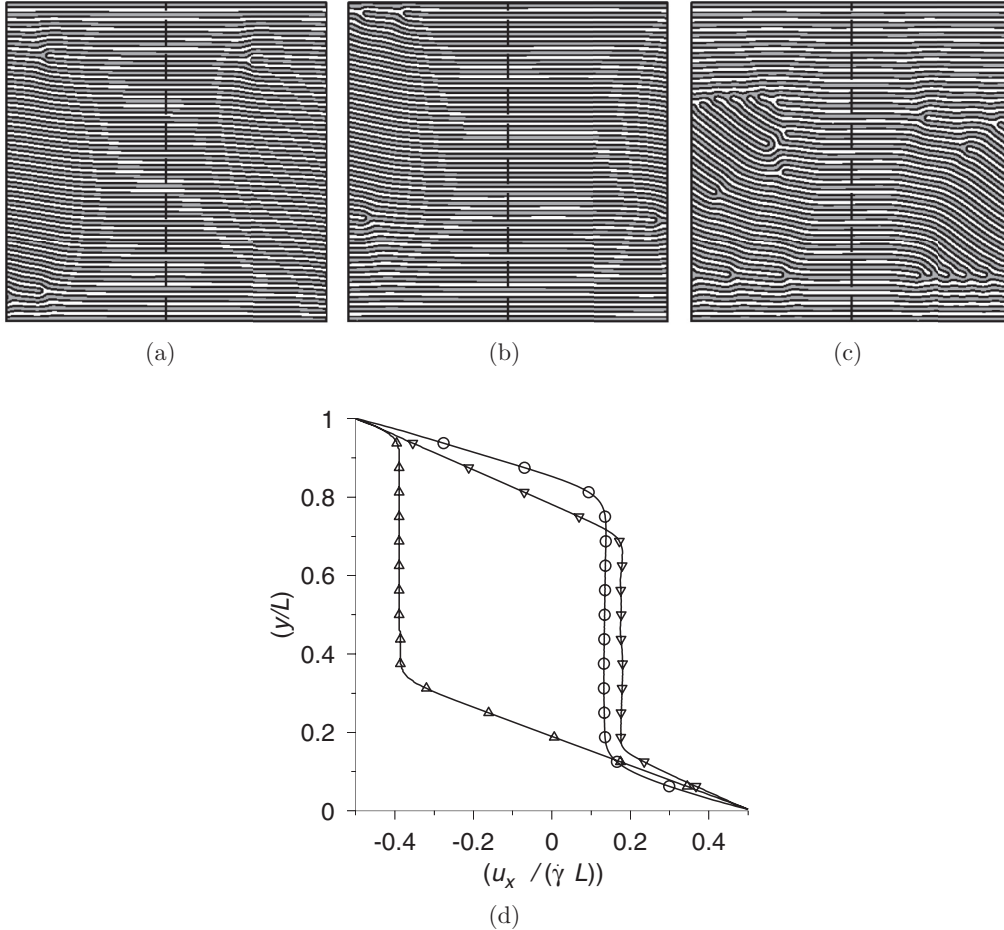


FIG. 15. The layer configurations at  $Er_0 = 4.9 \times 10^{-3}$ , and for (a)  $Sc_0 = 0.33$  and  $\dot{\gamma}t = 193.94$ , (b)  $Sc_0 = 1.0$  and  $\dot{\gamma}t = 203.55$ , and (c)  $Sc_0 = 5.0$  and  $\dot{\gamma}t = 310.06$ , and the scaled velocity profiles along the center of the simulation box in the streamwise direction (d) for  $Sc_0 = 0.33$  ( $\circ$ ),  $Sc_0 = 1$  ( $\Delta$ ), and  $Sc_0 = 5$  ( $\nabla$ ). In (a)–(c), the vertical dashed lines show the locations where the velocity profiles are evaluated. In (d), the bottom of the cell is at  $(y/L) = 0$ , and the top of the cell is at  $(y/L) = 1$ . In (a)–(c), the lines show contours of zero concentration.

Ericksen number). The root mean square of the concentration fluctuations  $\langle \psi^2 \rangle$  [Eq. (7)], not shown here for conciseness, reaches its equilibrium value in about 5 strain units, and the time taken is independent of the parameter  $r$ . This indicates that the amplitude of the concentration has quickly reached the equilibrium values shown in Fig. 28. However, the wavelength of the concentration field does not attain its equilibrium value even after 300 strain units. The reason for the persistent variation in the layer thickness for  $r \ll 1$  is as follows. From the concentration diffusion equation (A12), the concentration flux has contributions proportional to the Laplacian and the square of the Laplacian of the concentration field. For  $r \ll 1$ , the concentration field is close to a step function with sharp variations at the interface locations and nearly constant concentrations in the hydrophilic and hydrophobic phases, as shown in Fig. 28. The initial location of the interface seems to be a stochastic process during coarsening, resulting in lamellar phases with varying thickness of hydrophilic and hydrophobic parts. Once these are formed, there is very little driving force for a concentration flux within the hydrophilic and hydrophobic parts, since the concentration is nearly a constant at these locations. In fact, the dominant contributions to the flux in Eq. (A12) arise from the largest  $n$  contributions

when the expansion (A2) is used for the concentration field, since the flux contains terms proportional to  $n^2$  and  $n^4$ . The contribution to the flux due to the contribution  $n = 1$ , which captures the variations in the layer thickness, is relatively small. Since the driving force for equalizing layer thickness is small, it takes a long time for the layer spacing to alter and attain the equilibrium value. This can be seen by comparing Figs. 4 and 18. At  $r = 1$ , the system has attained local equilibrium and correct layer spacing at all  $Sc$ , whereas at  $r < 1$ , at the same dimensionless time ( $\dot{\gamma}t = 350$ ), we do not see local equilibrium ( $Sc_0 = 0.33$ ), or correct layer spacing ( $Sc_0 = 1, 5$ ).

### C. Viscosity contrast

Next, we study the effect of a variation in the viscosity between the hydrophilic and hydrophobic parts on the rheology of the system, using the model in Eq. (5). The structural evolution during the shear alignment for  $\mu_1 = 1.07$  and 2.13 (cases 10 and 11 in Table I) is shown in Fig. 21. The qualitative features are similar to those for the case of constant viscosity analyzed earlier. At  $Sc_0 = 0.33$ , the formation of misaligned domains is observed at  $\dot{\gamma}t = 20$  in Figs. 21(a) and 21(b)

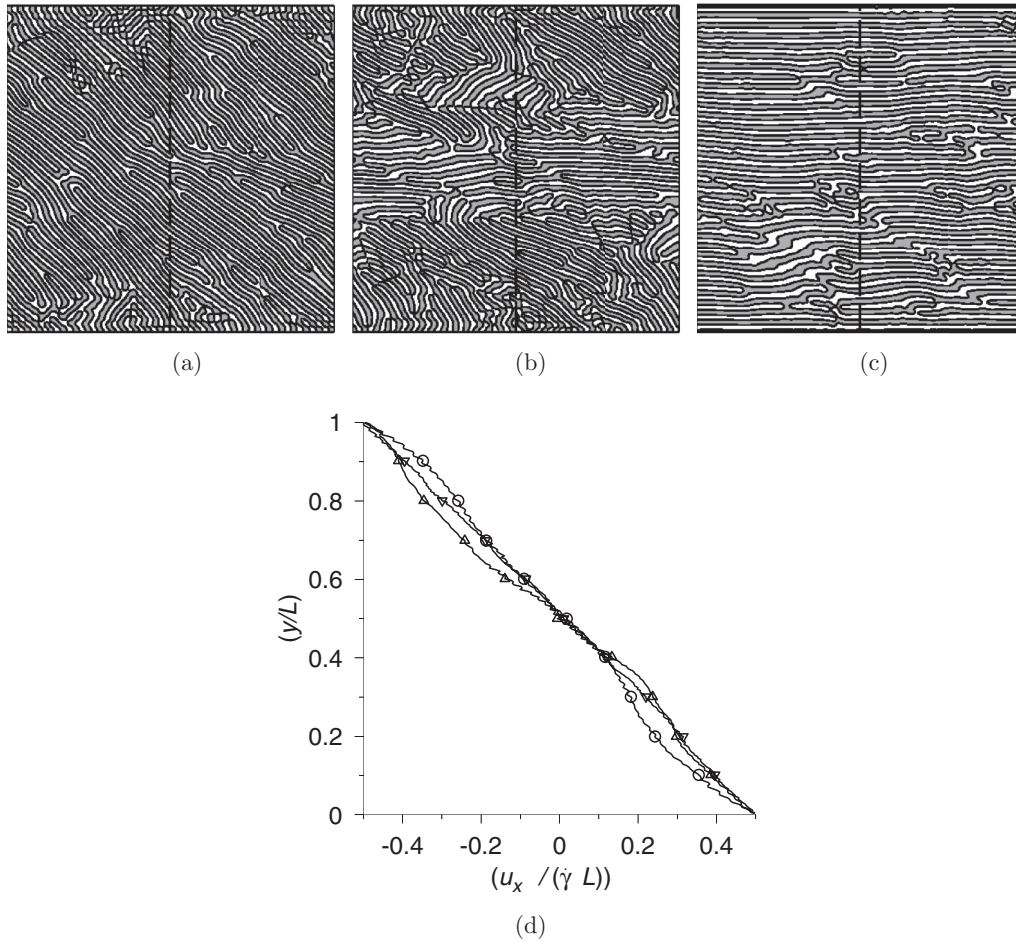


FIG. 16. The layer configurations at at  $Er_0 = 0.2$ , and (a)  $Sc_0 = 0.33$ ,  $\dot{\gamma}t = 50$ , (b)  $Sc_0 = 1.0$ ,  $\dot{\gamma}t = 20$ , and (c)  $Sc_0 = 5.0$  and  $\dot{\gamma}t = 5$ , and the scaled velocity profiles along the center of the simulation box in the streamwise direction (d) for  $Sc_0 = 0.33$  ( $\circ$ ),  $Sc_0 = 1$  ( $\Delta$ ), and  $Sc_0 = 5$  ( $\nabla$ ). In (a)–(c), the vertical dashed lines show the locations where the velocity profiles are evaluated. In (d), the bottom of the cell is at  $(y/L) = 0$ , and the top of the cell is at  $(y/L) = 1$ . In (a)–(c), the lines show contours of zero concentration.

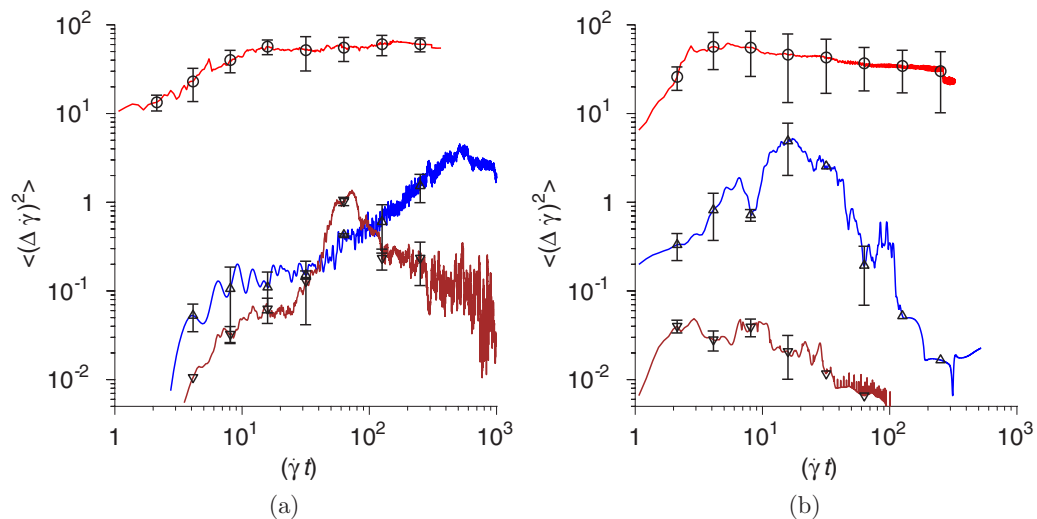


FIG. 17. The measure  $\langle (\Delta \dot{\gamma})^2 \rangle$  of the departure from a linear velocity profile as a function of time for  $Sc_0 = 0.33$  (a) and  $Sc_0 = 5$  (b) for  $Er_0 = 4.9 \times 10^{-3}$  (red,  $\circ$ ),  $Er_0 = 0.1$  (blue,  $\Delta$ ),  $Er_0 = 0.49$  (brown  $\nabla$ ). For  $Er_0 = 4.9$ , the value of  $\langle (\Delta \dot{\gamma})^2 \rangle$  is lower than  $10^{-3}$ .

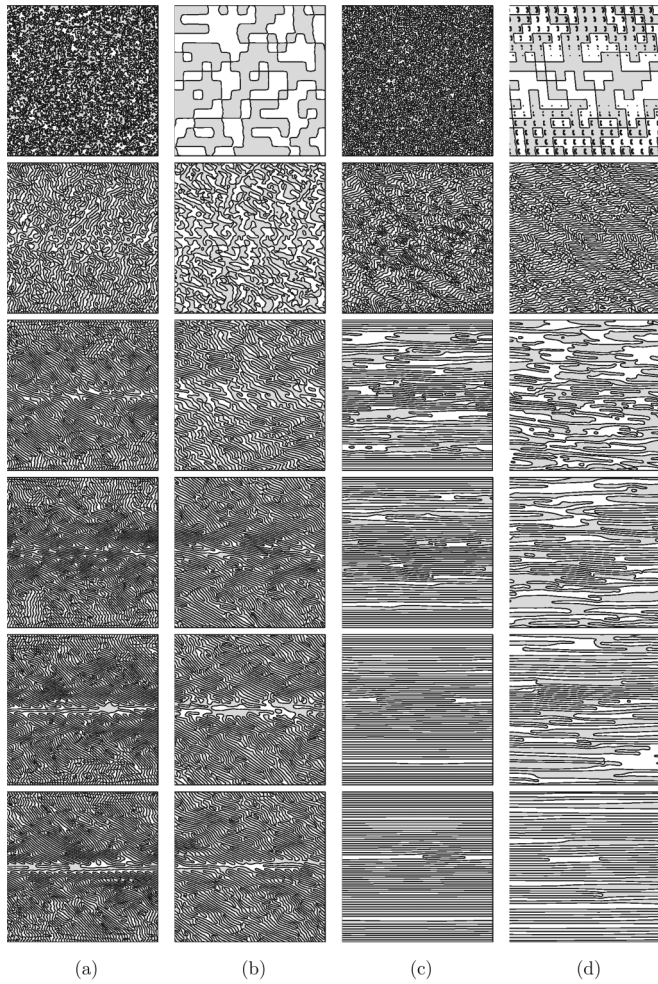


FIG. 18. Layer evolution for (a)  $r=0.1$ ,  $Sc_0=0.33$ , (b)  $r=0.01$ ,  $Sc_0=0.33$ , (c)  $r=0.1$ ,  $Sc_0=5$ , and (d)  $r=0.01$ ,  $Sc_0=5$ . Top to bottom,  $(\dot{\gamma}t) = 0.1, 5, 20, 50, 100$ , and  $350$ . The lines show contours of zero concentration.

for  $\mu_1 = 1.07$  and  $2.13$ . This is followed by the rotation at  $\dot{\gamma}t = 50$  and subsequent deformation (configurations at  $\dot{\gamma}t = 100$ ). Shear banding is observed at for  $\dot{\gamma}t > 100$ , where horizontally aligned layers coexist with layers aligned along the extensional axis, and further alignment takes place by the expansion of the zone with horizontally aligned layers and the shrinkage of layers aligned along the extensional axis. At  $Sc_0 = 5.0$ , there is bilayer melting ( $\dot{\gamma}t = 5$ ) and reformation ( $\dot{\gamma}t = 20$ ) in Figs. 21(c) and 21(d) for  $\mu_1 = 1.07$  and  $2.17$ . Thus, as in the case of a system with no viscosity contrast, the alignment mechanism changes from domain growth to melting and reformation as the Schmidt number is increased, at approximately the same Schmidt number based on the viscosity  $\mu_0$ .

The change in the ordering mechanism is confirmed by the plots of the order parameters  $f$  and  $f_y$  in Fig. 22, where the order parameters  $f$  and  $f_y$  are shown for different values of  $\mu_r$ . For  $Sc_0 = 0.33$ , the order parameter  $f_y$  is much larger than  $f$  at early times, indicating that the equilibrium layer spacing is attained relatively quickly, but the layer normal is not along the gradient direction. As time progresses, the values

of  $f$  and  $f_y$  are comparable, due to the shear banding where a significant fraction of the layers are aligned with layer normal along the gradient direction, though complete alignment is not observed even for the longest times (strain units of 1000) in the simulations. In contrast, for  $Sc_0 = 5.0$ , the values of  $f$  and  $f_y$  are comparable even at early times, indicating that the layers normals are aligned along the gradient direction even when the layers are not fully formed. The order parameters  $f$  and  $f_y$  decrease approximately as  $t^{-1}$  in the long time limit. Significantly, there is not much difference in the values of  $f$  and  $f_y$  as the viscosity contrast is increased from  $\mu_1 = 0$  to  $\mu_1 = 2$ ; in fact, there appears to be a slight decrease in the disorder as the viscosity contrast is increased.

The coarsening of the concentration variations is slower as the viscosity contrast increases. The root mean square of the concentration fluctuations,  $\sqrt{\langle \psi^2 \rangle}$ , is shown as a function of  $\dot{\gamma}t$  in Fig. 23. There is a systematic increase in the number of strain units required for the concentration to reach its final steady state value, from about 2 strain units for no viscosity contrast ( $\mu_1 = 0$ ) to about 10 strain units at high viscosity contrast ( $\mu_1 = 2.13$ ). Though the number of strain units required at  $\mu_1 = 2.13$  is not as large as that required at high Ericksen number in Fig. 11, there is a clear trend of increasing coarsening time as the viscosity contrast increases. However, the strain required for  $\sqrt{\langle \psi^2 \rangle}$  to evolve to its steady state value is much smaller than the alignment time as shown by the order parameters  $f$  and  $f_y$  in Fig. 22, or the time required for viscosity evolution discussed next. This suggests that layer alignment, and not the coarsening of the concentration field, influences the rheology at high viscosity contrast.

In contrast to the variation in the structural order parameters  $f$ ,  $f_y$  and the defect density, the average viscosity does show a dramatic increase with an increase in  $\mu_1$ , as shown in Fig. 24. There is very little change in the viscosity when the parameter  $\mu_1$  is increased from 0 to 0.53, but there is a significant increase in the viscosity, by orders of magnitude, when  $\mu_1$  is increased to 1.07 and 2.13. Despite the increase in magnitude, the qualitative dependence of the viscosity on the Schmidt number does not change significantly. For low Schmidt number, the viscosity does not decrease to that for an aligned system even after 1000 strain units, and the viscosity shows a nonmonotonic variation with time. For high Schmidt number, the viscosity decreases proportional to  $t^{-1}$ , in a manner similar to the decrease in  $f$  and the defect density. This suggests that while there is a correlation between the disorder or the defect density and the viscosity at each value of the viscosity contrast ( $\mu_1$ ), the ratio of the viscosity and the order parameter ( $f$  or defect density) increases sharply as the viscosity contrast is increased. Another salient feature is that there is not much variation in the average viscosity when  $\mu_1$  is 0.53 or less, there is a dramatic increase in the average viscosity of the disordered states when  $\mu_1$  increases to 1.07, and then there is not much increase when  $\mu_1$  increases from 1.07 to 2.13. This suggests that there are two distinct rheological states, one at low viscosity contrast and the other at high viscosity contrast, with little variation within each state and a large difference in viscosity (of about two orders of magnitude) between the two states.

There are two reasons for the very high viscosities when  $\mu_1$  is increased. First, for large  $\mu_1$ , the average viscosity of the aligned state (stress divided by strain rate) is much smaller than

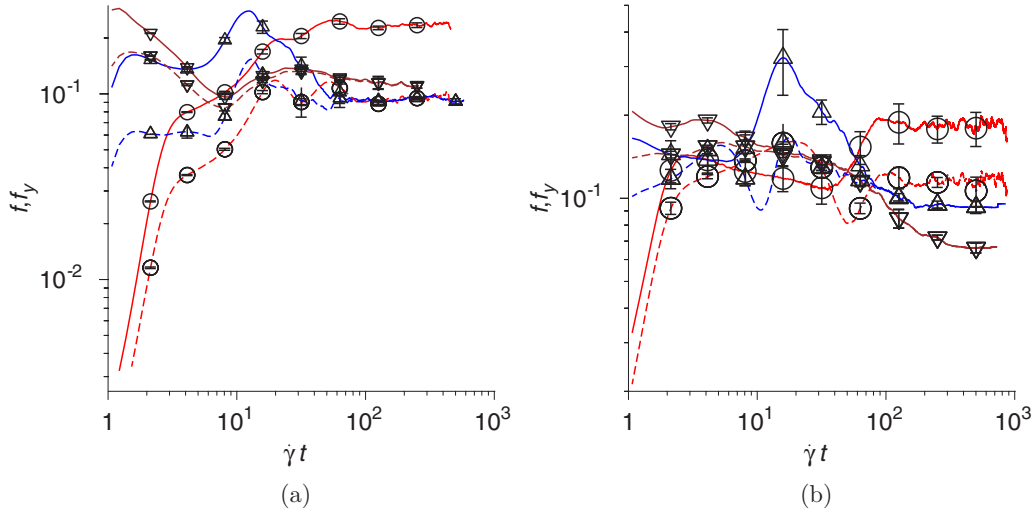


FIG. 19. The parameters  $f$  (solid lines) and  $f_y$  (dashed lines) for  $r = 0.01$  (a) and  $r = 0.1$  (b) for  $Er_0 = 0.2$ ,  $Sc_0 = 0.33$  (red,  $\circ$ ),  $Sc_0 = 1$  (blue,  $\Delta$ ), and  $Sc_0 = 5$  (brown,  $\nabla$ ). The equivalent plot for  $r = 1$  is given in Fig. 5.

$\mu_0$  in Eq. (5). As indicated in Table II, the ratio  $(\bar{\mu}/\mu_0)$  is 0.11 for  $\mu_1 = 1.07$ , and  $2.89 \times 10^{-2}$  for  $\mu_1 = 2.13$ , as evaluated using the inverse sum rule. For a disordered lamellar fluid, the viscosity is expected to scale with  $\mu_0$ , since it is necessary to strain the high viscosity regions to facilitate flow. Therefore, the ratio of the instantaneous viscosity (ratio of stress and strain rate) and the average viscosity of well-aligned layers is large at intermediate times for a disordered state. The other reason is the defect pinning mechanism, which results in a large resistance to deformation in solids and was previously observed at low Ericksen number. In the simulations, we observe that when there are even a small number of edge dislocations in the material, the region between the defects moves as a solid plug at constant velocity without straining, while the fluid strain rate is nonzero only over a part of the domain not pinned by the defects. This is illustrated in Fig. 25 for  $Sc_0 = 5.0$ , where the layer configurations are shown along with the velocity profiles across the center of the simulation cell in the streamwise direction. When there is no viscosity contrast, it is observed that there is a linear shear flow, even

though the configuration shown in Fig. 25(a) has substantial disorder. In contrast, for  $\mu_1 = 1.07$ , there is absence of shear in the regions where there are defects in the system, even though the number of defects is smaller for the configuration shown in Fig. 25(b) in comparison to that without viscosity contrast. In Fig. 25(c), we have chosen a configuration which has only two defects in it. Strikingly, it is observed that there is no shear in between the two defects at all in the velocity profile in Fig. 25(d). Due to this, the viscosity is very high until very late times when all the defects in the system are annealed. This indicates that the defect pinning mechanism in solids is operative when there is a significant variation in viscosity between the hydrophilic and hydrophobic parts. A similar feature is observed at low Schmidt number as well, as shown in Fig. 26. The configuration in Fig. 26(a) in the absence of viscosity contrast shows significant disorder. However, for this configuration, the velocity profile in Fig. 26(d) indicates that there is shearing throughout the bulk of the simulation box, though there is some departure from the linear velocity profile due to the disorder. In contrast, for the configurations

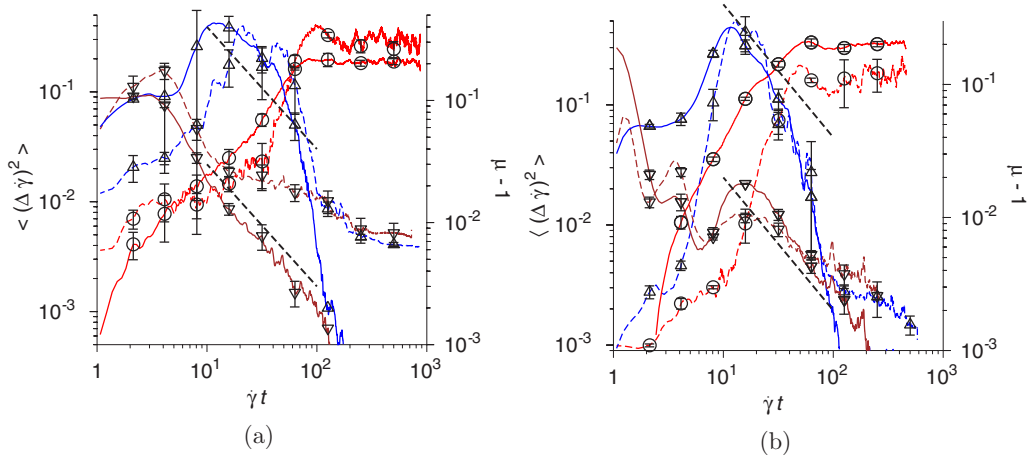


FIG. 20. The parameters  $\langle \Delta \dot{\gamma}^2 \rangle$  (dashed lines, left y axis) and  $\mu - 1$  (solid lines, right y axis) for  $r = 0.01$  (a) and  $r = 0.1$  (b) for  $Er_0 = 0.2$ ,  $Sc_0 = 0.33$  (red,  $\circ$ ),  $Sc_0 = 1$  (blue,  $\Delta$ ), and  $Sc_0 = 5$  (brown,  $\nabla$ ). The black dashed lines show a slope of  $-1$  on the log-log graph.

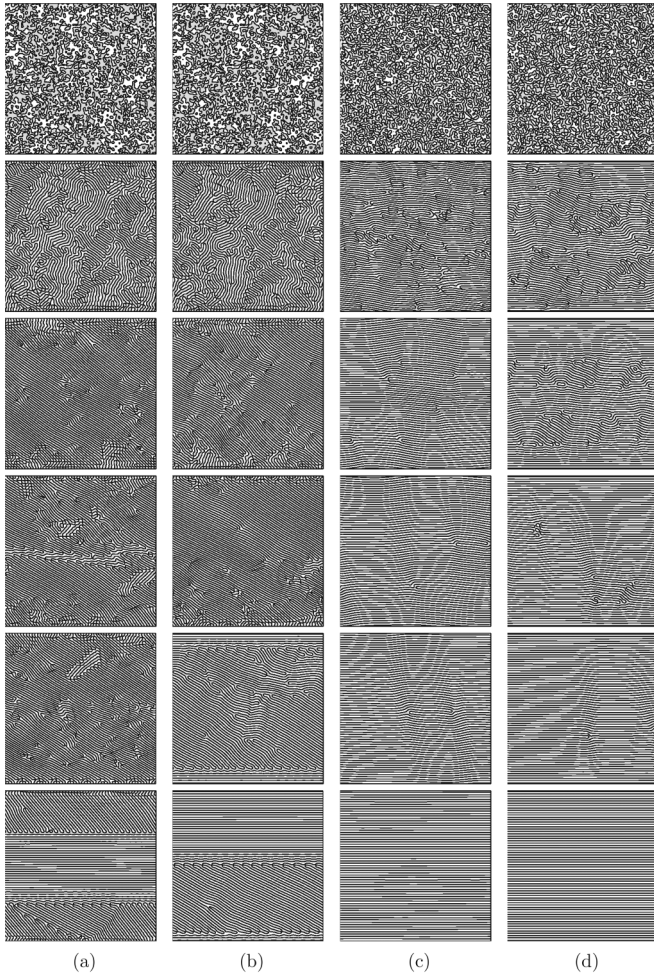


FIG. 21. Layer evolution for  $r = 1$ ,  $Er_0 = 0.2$ , (a)  $Sc_0 = 0.33$ ,  $\mu_1 = 1.07$ ; (b)  $Sc_0 = 0.33$ ,  $\mu_1 = 2.13$ ; (c)  $Sc_0 = 5$ ,  $\mu_1 = 1.07$ ; and (d)  $Sc_0 = 5$ ,  $\mu_1 = 2.13$ . Top to bottom,  $\tilde{\gamma}t = 0.1, 20, 50, 100, 500, 800$ . The lines show contours of zero concentration.

in Fig. 26(b) (for  $\mu_1 = 1.07$ ) and Fig. 26(c) (for  $\mu_1 = 2.13$ ), it is observed that the regions aligned along the extensional axis move as a block with no internal shearing, and there is shearing only in the regions where the layers are well aligned. This results in very large viscosities for the intermediate disordered configurations when there is a difference in viscosity between the hydrophobic and hydrophilic parts of the lamellar mesophase, and relatively low viscosity when there is no difference in the microscopic viscosity.

The parameter  $\langle \Delta \dot{\gamma}^2 \rangle$  [Eq. (12)], which provides a measure of the instantaneous departure of the velocity profile from the linear profile, is shown in Fig. 27. For low Schmidt number, the parameter  $\langle \Delta \dot{\gamma}^2 \rangle$  is significant even in the absence of viscosity contrast, due to the shear banding and the alignment of layers along the extensional axis at intermediate times. However, the parameter  $\langle \Delta \dot{\gamma}^2 \rangle$  does increase by a factor of about 5 as  $\mu_1$  is increased from 0 to 2.13, because the misaligned layers do not admit strain when the viscosity contrast is significant. For high Schmidt number,  $\langle \Delta \dot{\gamma}^2 \rangle$  at intermediate times is significantly higher, by a factor of 10 or more, when the parameter  $\mu_1$

increases from 0 to 2.13, even though the structure does not change, due to the lack of straining (plug flow) in the regions between defects for  $\mu_1 = 1.07$  and 2.13.

#### IV. CONCLUSIONS

A mesoscopic model has been used to examine the qualitative features of the evolution of viscosity under steady shear of an initially disordered lamellar mesophase. The important limitations in the simulation study are the relatively small size of the simulation box (about 32 times the layer spacing) and the restriction to two dimensions. These limitations arise due to the computational power required to carry out simulations, the requirement of reducing the lattice spacing to at most (1/8) of the layer spacing to resolve the concentration fields, and more notably due to the requirement of covering a large parameter space and carrying out multiple simulations for the same parameter set in order to obtain the standard deviations in the properties. The value of this study lies in the complete set of dimensionless parameters that have been identified which affect the rheology, based on the mesoscopic governing equations, and the qualitatively different types of flow behavior and structure-rheology relations that have been identified in different regimes.

The small system size limits the length scale of the disorder that is accessible in the simulations. Previous studies [13] have shown that the viscosity does depend on system size even for small systems. In experiments, the focal conic defects that are examined using polarizing microscopy have length scales  $10^3$ – $10^4$  times the layer spacing. Such large defect structures clearly cannot be studied in our simulations of modest size. The restriction to two dimensions limits the topological nature of the defects that can be observed to edge dislocations and misaligned domains with grain boundaries. The three-dimensional screw dislocations which are observed in experiments are not captured in the present simulations. Moreover, in three dimensions, the edge dislocations are not stable and they break up into focal-conic defects. All of these three-dimensional effects are not captured in the present simulations. The effect of screw dislocations is not likely to be significant under steady shear of hundreds of strain units, because a screw dislocation aligned in any direction cannot be deformed in a manner commensurate with a linear shear flow. In fact, edge dislocations are observed but screw dislocations are not observed in simulations of three dimensional shear flows [14,28], albeit of small system size. The important qualitative features observed here are not topologically restricted to two dimensions, and are likely to be observed in three dimensions as well, though the exact nature of the defects would change, for example, from edge dislocations in two dimensions to focal conic defects in three dimensions.

The objective of the present analysis is an extensive study of the effect of different dimensionless parameters on the process of alignment under shear. A comprehensive list of dimensionless parameters is enumerated on the basis of the free energy functional and the dynamical equations that govern the evolution of the coarse-grained concentration field which distinguishes between the hydrophilic and hydrophobic constituents of the lamellar fluid. With the exception of the Reynolds number, which is almost always low in practical

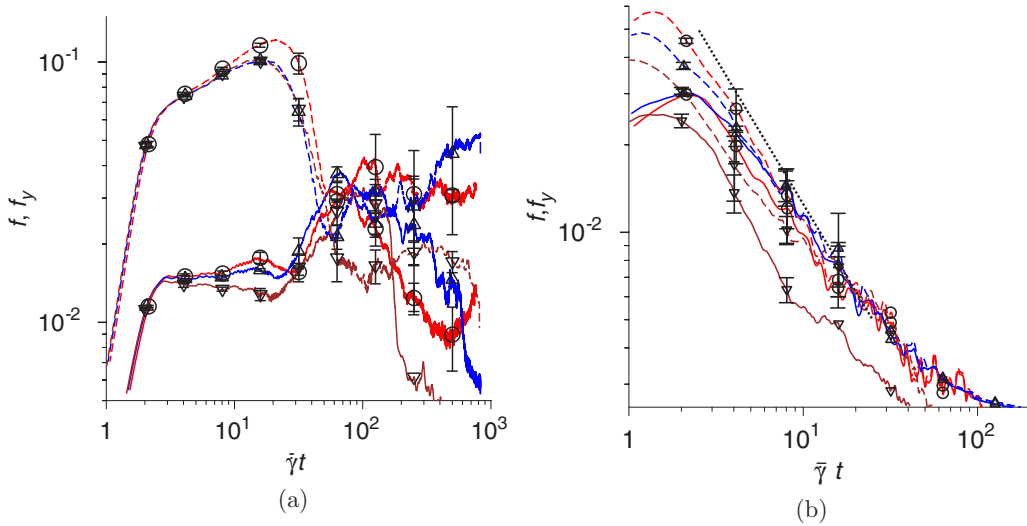


FIG. 22. The parameters  $f$  (solid lines) and  $f_y$  (dashed lines) as a function of  $\bar{\gamma}t$  for  $Sc_0 = 0.33$  (a) and  $Sc_0 = 5$  (b) for  $Er_0 = 0.2$ ,  $\mu_1 = 0$  (red,  $\circ$ ),  $\mu_1 = 1.07$  (blue,  $\Delta$ ), and  $\mu_1 = 2.13$  (brown,  $\nabla$ ). In (b), the dotted line shows a slope of  $-1$  on the log-log graph.

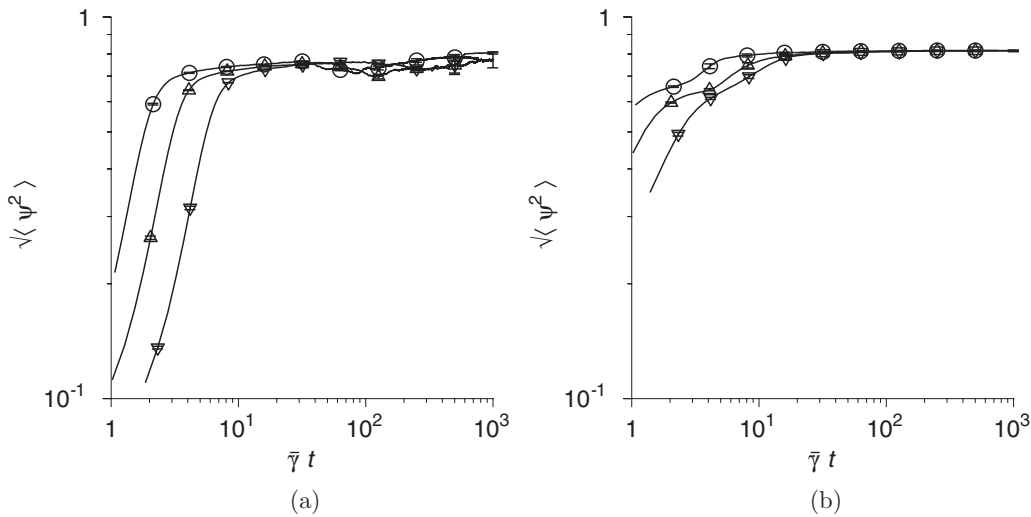


FIG. 23. The variation of the root mean square of the concentration averaged over the entire domain,  $\sqrt{\langle \psi^2 \rangle}$ , as a function of  $\bar{\gamma}t$  for  $\mu_1 = 0$  ( $\circ$ ),  $1.07$  ( $\Delta$ ), and  $2.13$  ( $\nabla$ ) for  $Sc_0 = 0.33$  (a) and  $Sc_0 = 5.0$  (b).

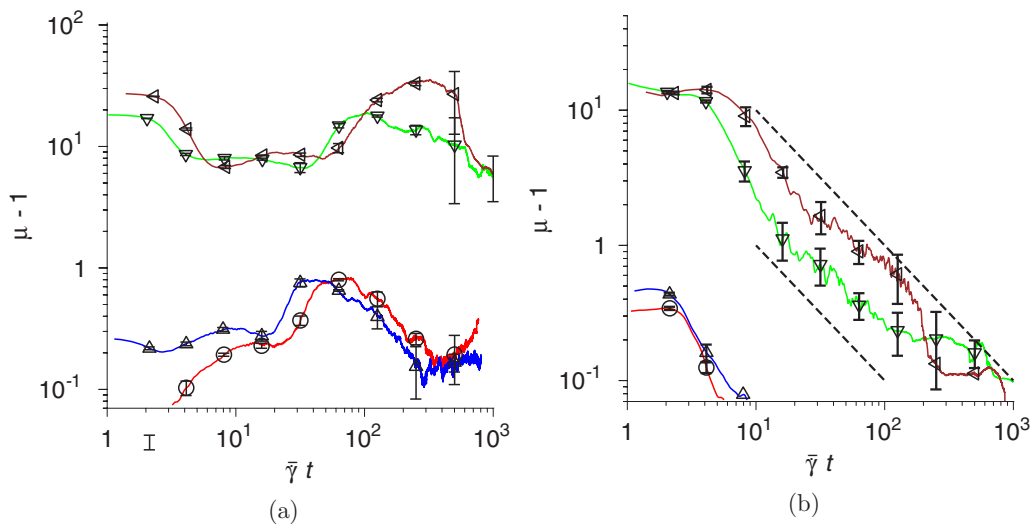


FIG. 24. The viscosity as a function of time for  $Sc_0 = 0.33$  (a) and  $Sc_0 = 5$  (b) for  $Er_0 = 0.2$ ,  $\mu_1 = 0$  (red,  $\circ$ ),  $\mu_1 = 0.53$  (blue,  $\Delta$ ),  $\mu_1 = 1.07$  (green,  $\nabla$ ) and  $\mu_1 = 2.13$  (brown,  $\triangleleft$ ). In sub-figure (b), the black dashed lines show a slope of  $-1$  on the log-log graph.

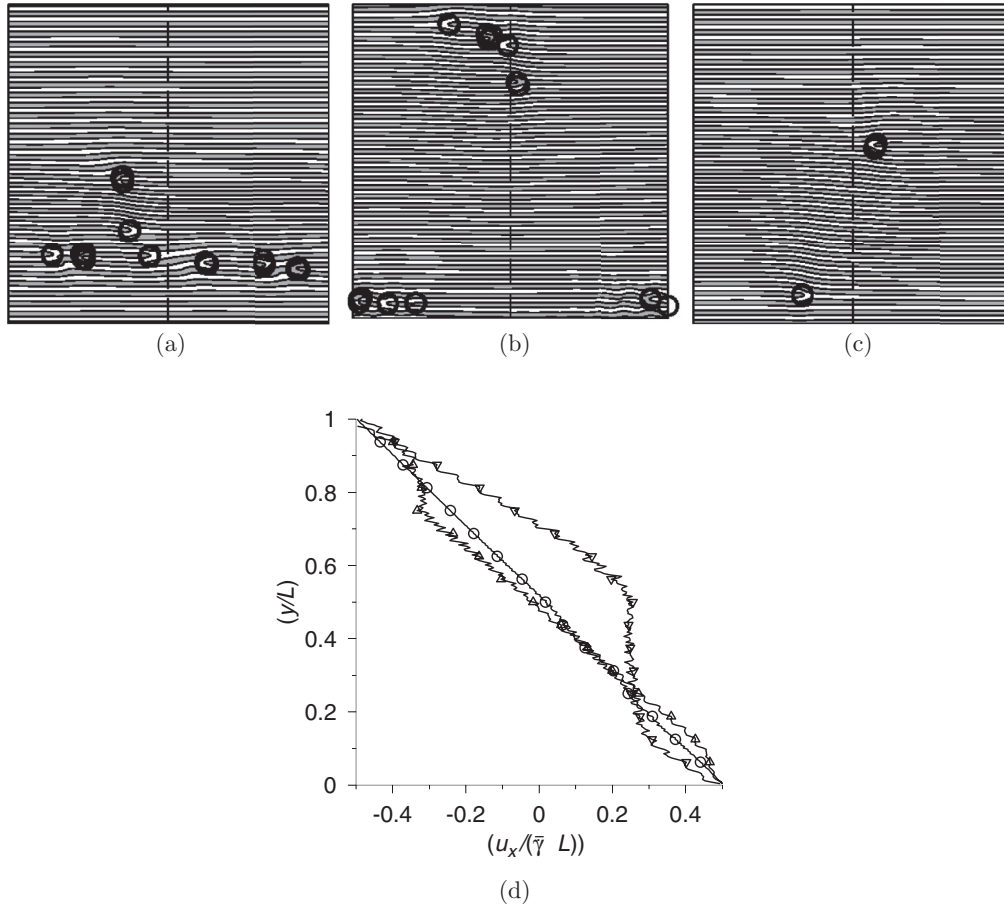


FIG. 25. The layer configurations at  $Er_0 = 0.2$ , and  $Sc_0 = 5.0$ , and (a)  $\mu_1 = 0$ ,  $\dot{\gamma}t = 56.61$ , (b)  $\mu_1 = 1.07$ ,  $\dot{\gamma}t = 81.67$ , and (c)  $\mu_1 = 2.13$ ,  $\dot{\gamma}t = 614.06$ , and the scaled velocity profiles along the center of the simulation box in the streamwise direction (d) for  $\mu_1 = 0$  ( $\circ$ ),  $\mu_1 = 1.07$  ( $\Delta$ ), and  $\mu_1 = 2.13$  ( $\nabla$ ). In (a)–(c), the vertical dashed lines show the locations where the velocity profiles are evaluated. In (d), the bottom of the cell is at  $(y/L) = 0$ , and the top of the cell is at  $(y/L) = 1$ . In (a)–(c), the lines show contours of zero concentration.

situations, the effects of variation in all other parameters are systematically studied. The parameters include the Schmidt number which is the ratio of momentum and mass diffusion, the Ericksen number which is a ratio of viscous and elastic forces, the interface sharpness parameters which is a measure of the ratio of the interface thickness (between the hydrophilic and hydrophobic parts) and the layer spacing, and the contrast in viscosity between the hydrophilic and hydrophobic parts. The methodology involves the definition of a set of parameters which provide quantitative measures of the layer alignment, the extent of segregation between hydrophilic and hydrophobic constituents, a measure of the number of defects in the system, and the macroscopic sample viscosity.

Different types of structure and viscosity evolution are observed in steady shear in different parameter regimes. The first two items listed below confirm the observations in the previous study [13], where simulations were carried out on smaller systems and the time dependence of the viscosity decrease was not evident, while the remaining items are new observations of the present analysis.

(1) At low Schmidt number, mass diffusion is fast compared to momentum diffusion. There is rapid formation of layered domains locally which are randomly oriented and not aligned with the global shear. The domains with layers aligned along

the extensional axis grow in comparison to those aligned along the compressional axis during coarsening, and in the long time limit domains aligned along the extensional axis are consistently found to coexist with layers with unit normal along the velocity gradient direction, as shown in Fig. 4(a). The system does not fully align even after it is deformed through many hundreds of units of strain, as shown by the order parameters in Fig. 5. The intermediate states with layers aligned along the extensional axis have very high resistance to flow, and so there is a large initial increase in the macroscopic viscosity (ratio of stress and strain rate), and the viscosity does not decrease to that for the well-aligned state even after hundreds of strain units, as shown in Fig. 6. There is a creation of defects due to shear. Two mechanisms have been identified earlier, the buckling instability due to expansion of layers along the extensional axis and the compressional instability along the compressional axis [13]. The physical mechanism of defect creation has also been analyzed [24].

(2) In contrast, at high Schmidt number, where momentum diffusion is fast compared to mass diffusion, the shear tends to break and reform the layers, resulting in configurations where the layer normal is aligned in the gradient direction even at very early times. This results in configurations where isolated edge

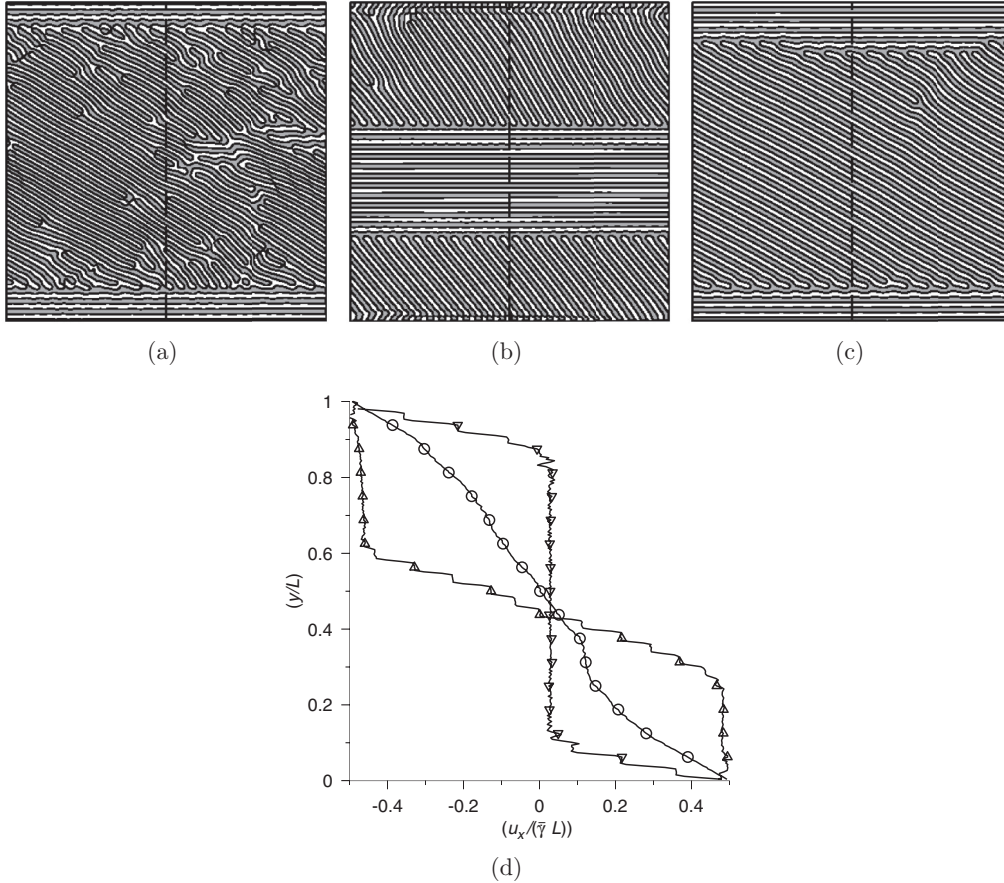


FIG. 26. The layer configurations for  $Er_0 = 0.2$ ,  $r = 1$ , and  $Sc_0 = 0.33$  for (a)  $\mu_1 = 0$ ,  $\bar{\gamma}t = 87.43$ , (b)  $\mu_1 = 1.07$ ,  $\bar{\gamma}t = 997.86$ , and (c)  $\mu_1 = 2.13$ ,  $\bar{\gamma}t = 2648.6$ ; and the scaled velocity profiles along the center of the simulation box in the streamwise direction (d) for  $\mu_1 = 0$  ( $\circ$ ),  $\mu_1 = 1.07$  ( $\Delta$ ), and  $\mu_1 = 2.13$  ( $\nabla$ ). In (a)–(c), the vertical dashed lines show the locations where the velocity profiles are evaluated. In (d), the bottom of the cell is at  $(y/L) = 0$ , and the top of the cell is at  $(y/L) = 1$ . In (a)–(c), the lines show contours of zero concentration.

dislocations are observed in a background well-aligned lamellar phase, resulting in a lower resistance to flow and a lower viscosity, as shown in Fig. 4(c). The time required for complete alignment decreases as the Schmidt number is increased. At moderate and high Schmidt numbers, the difference between the instantaneous viscosity (ratio of stress and strain rate) and the viscosity for a well-aligned state decreases proportional to  $t^{-1}$  (or the inverse of the number of strain units) in the long time limit, as shown in Fig. 6. This scaling law was predicted if the alignment is due to the cancellation of edge dislocations of opposite Burgers vectors due to the shear flow [24], and this scaling law is consistently observed in the simulations at moderate and high Schmidt numbers.

(3) At high Ericksen number, where the viscous forces are large compared to the elastic restoring forces, the shear flow tends to homogenize the concentration fluctuations in the disordered state, resulting in incomplete segregation between the hydrophilic and hydrophobic components, as shown in Figs. 8 and 9. The amplitude of the concentration fluctuations increases to its equilibrium value only after 50–100 units of strain at  $Er_0 = 4.9$ , and the equilibrium concentration profiles are not observed even after 1000 units of strain at  $Er_0 = 490$ , as shown by the measure  $\sqrt{\langle \psi^2 \rangle}$  in Fig. 11. At low Schmidt number and high Ericksen number, the layers

are not completely formed, and there appears to be a pearling instability of the layers which prevents layer formation, as shown in Fig. 8. This results in a decrease in the macroscopic viscosity during the shear alignment as the Ericksen number is increased, as shown in Fig. 10.

(4) At low Ericksen number, where viscous forces are small compared to elastic restoring forces, the formation of misaligned domains is observed initially during shearing, followed by the transition to a nearly well aligned state with edge dislocations. However, due to the high stiffness of the layers, the defects do not anneal completely even after shearing for hundreds of strain units at  $Er_0 = 4.9 \times 10^{-3}$  as shown in Fig. 12. The high stiffness of the layers prevents the glide motion of the defects perpendicular to the layers, which is required for the motion and cancellation of defects. The defect-pinning mechanism, where regions between defects move as a block without shearing, is also observed at low Ericksen numbers, as shown in Fig. 15. When defect pinning takes place, there is straining only in a small part of the domain, and this results in a significant increase in the macroscopic viscosity as the Ericksen number is decreased, as shown in Fig. 14.

(5) The defect pinning mechanism is also found to be operative when there is a significant difference in viscosity between the hydrophilic and hydrophobic constituents, as

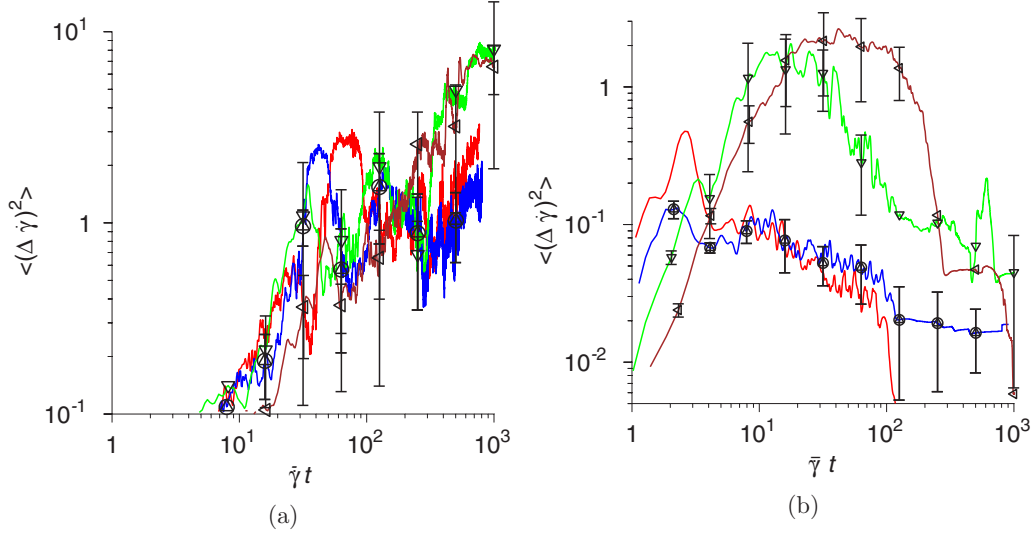


FIG. 27. The measure  $\langle (\Delta \dot{\gamma})^2 \rangle$  of the departure from a linear velocity profile as a function of time for  $Sc_0 = 0.33$  (a) and  $Sc_0 = 5$  (b) for  $Er_0 = 0.2$ ,  $\mu_1 = 0$  (red,  $\circ$ ),  $\mu_1 = 0.53$  (blue,  $\diamond$ ),  $\mu_1 = 1.04$  (green,  $\triangle$ ), and  $\mu_1 = 2.13$  (brown,  $\nabla$ ).

shown in Fig. 25, resulting in a significant increase in the macroscopic viscosity, as shown in Fig. 24. There is a modest delay of up to 5 strain units in the development of the concentration modulation at high viscosity contrast, as shown indicated by the measure  $\sqrt{\langle \psi^2 \rangle}$  in Fig. 23, but this does not seem to significantly affect the dynamics.

However, we do not observe any viscous fingering instability, even at the highest viscosity contrast considered here. Viscous fingering is usually observed in a pressure driven flow through a porous medium or in thin channels. It is an open question whether this will be observed at still higher viscosity contrasts between the hydrophilic and hydrophobic parts.

(6) A decrease in the parameter  $r$  in the free energy functional 1, which results in a decrease in the width of the interface between the hydrophilic and hydrophobic parts (in comparison to the wavelength of the equilibrium concentration modulation) leads to a larger variation in the layer spacing even at long times. Layers initially form stochastically with spacing different from the equilibrium spacing, as shown in Fig. 18. In these layers, the concentration profile resembles a step profile, and the concentration is nearly a constant within the hydrophobic and hydrophilic parts of the bilayer, with a rapid variation in concentration between the two. Since there is a driving force for diffusion only in the regions with gradients in the concentration field, the driving force for diffusion is present only in a small part of the domain. This results in a reduction in the flux, and the variations in the layer spacing is permitted even after a few hundreds of strain units. Despite the increased disorder, the viscosity decreases as the parameter  $r$  is decreased or the interface becomes sharper, as shown in Fig. 20.

The above qualitative features are likely to be observed in real systems as well, since they are not limited to two dimensions. For lyotropic lamellar systems, the prominent contribution to the high viscosity is likely to be due to the high viscosity contrast between the hydrophilic and hydrophobic parts, which results in defect pinning and an increase in viscosity increase by up to two orders of magnitude in comparison to the well aligned state.

## ACKNOWLEDGMENTS

The authors would like to thank the Department of Science and Technology, Government of India for financial support, and Supercomputer Education and Research Centre (SERC) at Indian Institute of Science for the computational resources.

## APPENDIX A: MESOSCALE DESCRIPTION

The free energy governing the concentration field is given in Eq. (1). The parameter  $A$  is an energy density, which determines the compression and bending moduli in the free energy (2) expressed in terms of the displacement field, as shown below. The wave number  $k = (2\pi/\lambda)$ , where  $\lambda$  is the wavelength of the concentration modulations. The parameter  $r$  determines the interface thickness between the hydrophilic and hydrophobic parts. For  $r \gg 1$ , the concentration profile is close to a sinusoidal profile, while for small  $r$ , the concentration profile resembles a step function, as shown in Fig. 28. The value of the parameter  $g$  is adjusted to ensure that the lamellar phase has zero surface tension, as expected from symmetry.

At equilibrium, the free energy is minimum and the concentration field satisfies the equation

$$\frac{\delta F}{\delta \psi} = A \left( -\psi + \psi^3 - \frac{g}{k^2} \nabla^2 \psi + \frac{r}{k^4} (\nabla^4 + 2k^2 \nabla^2 + k^4) \psi \right) = 0. \quad (\text{A1})$$

For a lamellar mesophase with layers in the  $x$ - $z$  plane and the layer normal along the  $y$  axis, the most general solution for Eq. (A1) is

$$\psi = \sum_{n=-\infty}^{\infty} \psi_n \exp(inky). \quad (\text{A2})$$

This general form of  $\psi$  Eq. (A2) is inserted in Eq. (A1) and the coefficients of  $\exp(inky)$  for each value of  $n$  are equated to zero to calculate  $\psi_n$  as a function of  $r$ . Since the concentration field is real and the average concentration is zero

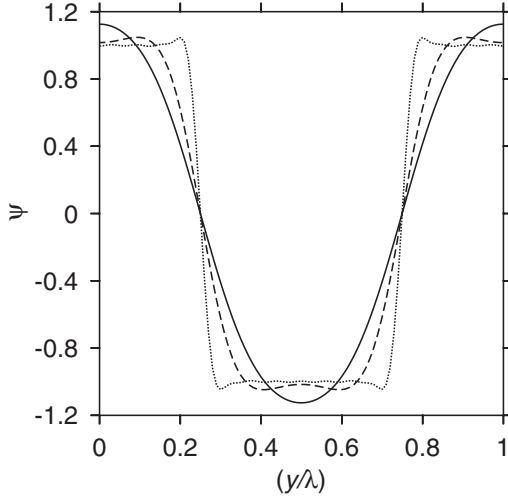


FIG. 28. Equilibrium profiles for the concentration field  $\psi$  as a function of  $(y/\lambda)$  for values of parameter  $r$  chosen in this study, namely  $10^{-4}$  (dotted line),  $10^{-2}$  (dashed line), and 1 (solid line). Here,  $\lambda$  is the wavelength of the concentration modulations and  $y$  is the direction perpendicular to the layers.

for a symmetric lamellar mesophase,  $\psi_{-n} = \psi_n$  and  $\psi_0 = 0$ . For large  $r$ , Eq. (A1) reduces to  $[(\partial^2/\partial y^2) + k^2]\psi = 0$ , and the equilibrium solution for  $\psi$  has a sinusoidal spatial variation with wavelength  $(2\pi/k)$ . In contrast, for  $r \ll 1$  and small  $g$ ,  $-\psi + \psi^3 = 0$  indicates concentration profile is a step function. Hence, with decreasing  $r$ , there is a transition from a sinusoidal interface to one with a steep gradient between the hydrophilic and hydrophobic parts, as shown in Fig. 28. A detailed analysis [22] shows that the coefficients in Eq. (A2) scale as  $\psi_n \propto r^{-(n-1)/2}$  for  $r \gg 1$ . In the opposite limit ( $r \ll 1$ ), the interface thickness is proportional to  $(r^{1/4}/k)$ , and  $\psi_n \propto n^{-1}$  for  $n \leq n_c = r^{-1/4}$  [22] where  $n_c$  is the cutoff for the expansion in Eq. (A2). The cutoff for  $n$  arises in the case of  $r \ll 1$ , because for nonzero but small  $r$ , the terms proportional to  $r$  in Eq. (A1) become comparable to the other terms when  $n \sim r^{-1/4}$ . The effect of the steepness of the interface, through the parameter  $r$ , on the shear alignment is one of the parametric studies carried out here.

The free energy functional  $F[u]$  could be obtained from the free energy functional  $[F[\psi]]$  in Eq. (1), by perturbing the equilibrium concentration field in Eq. (A2) as

$$\psi = \sum_{n=-\infty}^{\infty} \psi_n \exp\{ink[y - u(\mathbf{x}, t)]\}. \quad (\text{A3})$$

A series expansion in the displacement  $u(\mathbf{x}, t)$  is used, linear and quadratic terms in the expansion are retained, and the resultant equation is compared with Eq. (2) to get the expressions for  $B, G, K$  in terms of mesoscale parameters  $(A, g, r)$ . The results are of the form [22]

$$B = A \sum_{n=-\infty}^{\infty} [2rn^2(3n^2 - 1) + gn^2]\psi_n^2, \quad (\text{A4})$$

$$G = A \sum_{n=-\infty}^{\infty} [2rn^2(n^2 - 1) + gn^2]\psi_n^2, \quad (\text{A5})$$

$$K = A \sum_{n=-\infty}^{\infty} (rn^2/k^2)\psi_n^2. \quad (\text{A6})$$

For Eq. (A5), it is clear that the parameter  $g$  at mesoscale has to be set to a negative value, given by

$$g = -\frac{\sum_{n=-\infty}^{\infty} [2rn^2(n^2 - 1)]\psi_n^2}{\sum_{n=-\infty}^{\infty} n^2\psi_n^2}, \quad (\text{A7})$$

for the surface tension to be zero at macroscale.

From Eq. (A6), the bending modulus  $K$  depends only upon parameters  $A$ ,  $r$ , and  $k$  in free energy functional (1), while the compression modulus depends only on  $A$  and  $r$ . For  $r \gg 1$ ,  $\psi_n \propto r^{-(n-1)/2} \exp(-an)$  for large  $r$  and  $n$ , where  $a$  is a constant. Consequently, the expressions for the bending and compression moduli, Eqs. (A6) and (A4), are dominated by the first terms in the expansion,

$$K \sim \frac{Ar}{k^2}; \quad B \sim Ar. \quad (\text{A8})$$

In limit  $r \ll 1$ , for  $n \leq n_c = r^{-1/4}$ ,  $\psi_n \propto n^{-1}$ , and from Eq. (A6),

$$K \sim A \frac{r}{k^2} n_c \sim A \frac{r^{3/4}}{k^2}; \quad B \sim Arn_c \sim Ar^{3/4}. \quad (\text{A9})$$

The parameter  $A$  has been varied in present study to the differences in layer alignment and rheology for different values of the compression and bending moduli.

The dynamical equations, for concentration ( $\psi$ ) and velocity ( $\mathbf{v}$ ) fields, are [7]

$$\frac{\partial \psi}{\partial t} + \nabla \cdot (\mathbf{v}\psi) = \Gamma \nabla^2 \left( \frac{\delta F}{\delta \psi} \right), \quad (\text{A10})$$

$$\nabla \cdot \mathbf{v} = 0, \quad (\text{A11})$$

$$\rho \left( \frac{\partial \mathbf{v}}{\partial t} + \mathbf{v} \cdot \nabla \mathbf{v} \right) = -\nabla p + \nabla \cdot \{ \mu' [\nabla \mathbf{v} + (\nabla \mathbf{v})^T] \} + (\nabla \psi) \frac{\delta F}{\delta \psi}. \quad (\text{A12})$$

Equation (A10) is the convection-diffusion equation for the concentration field, where  $\Gamma$ , the Onsager coefficient, is related to mass diffusivity  $D$ . Equation (A11) is the mass balance condition for incompressible fluid, and Eq. (A12) is the momentum balance equation. The left side in Eq. (A12) represents inertial terms, and  $\rho$  is the fluid density. The first two terms on the right side are the divergence of the pressure  $p$ , and the divergence of Newtonian stress tensor, where  $\mu'$  is the coefficient of viscosity. It should be noted that one of the dependencies studied in the present analysis is the dependence of the coefficient of viscosity on the concentration, and so the viscosity  $\mu'$  is not a constant. The last term on the right of Eq. (A12) is the divergence of an additional stress which arises due to chemical potential gradients, and which is required to ensure that the concentration and momentum equations satisfy the Poisson bracket relations. Thermal fluctuations are neglected in Eqs. (A10) and (A12), since we consider the zero temperature limit where ordering occurs only due to the imposed shear flow.

In a ‘‘macroscale’’ description for a nearly aligned system near equilibrium, the governing equations are employed for layer displacement field  $u$  and for the fluid velocity field. Here,  $u$  is the displacement, in the direction perpendicular to the layers, about an equilibrium lamellar configuration. A perturbation in an aligned lamellar configuration causes a restoring force which results in movement of the layers relative to the surrounding fluid. The permeation of the fluid through the layers causes an opposing drag force proportional to the difference in layer and fluid velocity (in a manner similar to the Darcy law for flow through porous media). The equation for the layer displacement  $u$  in the  $y$  direction is [22]

$$\begin{aligned} \frac{\partial u}{\partial t} - v_y &= -P \frac{\delta F[u]}{\delta u} \\ &= P \left( B \frac{\partial^2 u}{\partial y^2} - K \left( \frac{\partial^2}{\partial x^2} + \frac{\partial^2}{\partial z^2} \right)^2 u \right). \end{aligned} \quad (\text{A13})$$

The left side of the above equation is the difference between the layer velocity and the fluid velocity in the direction perpendicular to the layers. On the right, the term,  $-\frac{\delta F}{\delta u}$  represents the restoring force density, and  $P$  is the permeation constant. The two terms on the right side of Eq. (A13) are the force densities due to layer compression and bending respectively. The force due to the relative motion between the fluid and layers results in an additional term in the momentum equation for the fluid in the direction perpendicular to the layers,

$$\rho \left( \frac{\partial \mathbf{v}}{\partial t} + \mathbf{v} \cdot \nabla \mathbf{v} \right) = -\nabla p + \nabla \cdot \{ \mu' [ \nabla \mathbf{v} + (\nabla \mathbf{v})^T ] \} + \frac{\delta F}{\delta u} \mathbf{n}, \quad (\text{A14})$$

where  $\mathbf{n}$  is the direction perpendicular to the layers. Equations (A13) and (A14) along with the mass balance condition [Eq. (A11)] complete the description of lamellar phase systems at macroscale. Equations (A13) and (A14) can be obtained by inserting the perturbed concentration field in Eq. (A3) into Eqs. (A10) and (A12). The resulting equations are simplified by keeping only the term linear in  $u$  and  $\mathbf{v}$  during the expansion,

TABLE I. List of values of various dimensionless numbers and parameters used in the simulations of system size equal to 32 times the layer spacing in the streamwise and cross-stream directions. The value of  $\text{Re}_0$  is set equal to 1 in all cases, and the value of  $\text{Sc}_0$  is set to values of 0.33, 0.66, 1.0, 2.0, and 5.0.

Case	$\text{Er}_0$	$r$	$\mu_1$
1	0.2	1.0	0
2	4.9	1.0	0
3	0.49	1.0	0
4	0.1	1.0	0
5	$4.9 \times 10^{-3}$	1.0	0
6	0.2	0.1	0
7	0.2	0.01	0
8	0.2	1.0	0.32
9	0.2	1.0	0.53
10	0.2	1.0	1.07
11	0.2	1.0	2.13

TABLE II. The parameters  $\mu_1$  [Eq. (5)] used in the simulations, and the corresponding ratio of  $(\bar{\mu}/\mu_0)$  [Eq. (6)], the ratio of the difference between maximum and minimum viscosities  $\Delta\mu$ , and the average viscosity  $\mu_0$ , and the ratios of the Reynolds, Schmidt, and Ericksen numbers based on  $\bar{\mu}$  and  $\mu_0$ .

$\mu_1$	$\bar{\mu}/\mu_0$	$\Delta\mu/\bar{\mu}$	$(\text{Re}_{\bar{\mu}}/\text{Re}_0)$ $(\text{Sc}_0/\text{Sc}_{\bar{\mu}})$ $(\text{Er}_0/\text{Er}_{\bar{\mu}})$
0.0	1.00	0.00	1.00
0.32	0.95	0.63	1.05
0.53	0.86	1.16	1.16
1.07	0.11	17.90	9.00
2.13	$2.89 \times 10^{-2}$	103.38	34.60

to obtain a relation between the Onsager coefficient and permeation constant,

$$P = \frac{\Gamma}{\sum_{-\infty}^{\infty} \psi_n^2}. \quad (\text{A15})$$

Since  $\psi_n \sim n^{-1}$  when  $r \ll 1$ ,  $P$  is approximately equal to  $\Gamma$ . The ratio  $(P/\Gamma)$  tends to 1.5 for  $r \gg 1$  [22]. Also, from Eq. (A13),  $P B \sim D$ , where  $D$  is diffusion coefficient.

The set of parameters used in the simulations is shown in Table I. For each of these parameter sets, the Reynolds number based on the viscosity  $\mu_0$  is set equal to 1, and the Schmidt number  $\text{Sc}_0$  based on the viscosity  $\mu_0$  is set to values of 0.33, 0.66, 1.0, 2.0, and 5.0. The relation between the average viscosity  $\bar{\mu}$  and the viscosity  $\mu_0$  in Eq. (5) is given in Table II.

## APPENDIX B: LATTICE BOLTZMANN SIMULATIONS

In kinetic theory [29], the Boltzmann equation,

$$\frac{\partial f}{\partial t} + \mathbf{e} \cdot \frac{\partial f}{\partial \mathbf{x}} + \mathbf{a} \cdot \frac{\partial f}{\partial \mathbf{e}} = \frac{\partial_c f}{\partial t}, \quad (\text{B1})$$

describes evolution of the particle distribution function,  $f(\mathbf{x}, \mathbf{e}, t)$ , where  $f(\mathbf{x}, \mathbf{e}, t) d\mathbf{x} d\mathbf{e}$  is the probability of finding a particle in differential volume  $d\mathbf{x} d\mathbf{e}$  around location  $\mathbf{x}$  and velocity  $\mathbf{e}$  in phase space  $(\Gamma)$ , and  $\mathbf{a}$  is acceleration on the particles. The important assumption here is the molecular chaos approximation which states that the particle velocities are uncorrelated before collision. The terms on the left hand side of Eq. (B1) denote free streaming in phase space and  $\frac{\partial_c f}{\partial t}$  is the collision integral which accounts for binary collisions between particles. Due to the form of the collision integral term it is difficult solve the integrodifferential Boltzmann equation except in special cases. Different approximations, known as collision models, have been proposed over the years for the collision integral term to make the Boltzmann equation amenable to analytical and computational treatment.

In single relaxation lattice Boltzmann simulations, we solve

$$f_i(\mathbf{x} + \mathbf{e}_i, t + 1) - f_i(\mathbf{x}, t) = -\frac{f_i - f_i^{\text{eq}}}{\tau_f}, \quad (\text{B2})$$

which is a peculiar discretization of Boltzmann equation, with the Bhatnagar-Gross-Krook (BGK) [30] collision model, in physical  $(\mathbf{x})$  and in velocity  $(\mathbf{e})$  space. As before, the left side represents streaming where particles, which now can have only

discrete velocities  $\{\mathbf{e}_i\}$ , move from one lattice site ( $\mathbf{x}$ ) to another ( $\mathbf{x} + \mathbf{e}_i$ ) in unit time ( $\Delta t = 1$ ). The BGK collision term (right side) relaxes the system towards local equilibrium, where  $\tau_f$  is relaxation time parameter. The macroscopic quantities such as mass density, velocity, stress, etc., could be obtained by taking the appropriate moment of distribution function, e.g.,

$$\begin{aligned} \sum_i f_i &= \rho, \\ \sum_i f_i e_{i\alpha} &= \rho v_\alpha. \end{aligned} \quad (\text{B3})$$

The additional force density for nonideal fluids could be either included as an extra term in the right hand side of Eq. (B2) or incorporated in equilibrium distribution function. We have used the latter method in the present simulations. The  $f_i^{\text{eq}}$  is then given as

$$\begin{aligned} f_i^{\text{eq}}(\mathbf{x}, \mathbf{v}) &= \rho [A_1^i + A_2^i(\mathbf{v} \cdot \mathbf{e}_i) + A_3^i(\mathbf{v} \cdot \mathbf{e}_i)^2 \\ &\quad + A_4^i(\mathbf{v} \cdot \mathbf{v}) + (\mathbf{G} : \mathbf{e}_i \mathbf{e}_i)]. \end{aligned} \quad (\text{B4})$$

The tensor  $\mathbf{G}$  incorporates the additional contributions to Newtonian stress tensor, in this case due to concentration variations. The coefficients  $A_j^i (j = 1-4)$  and tensor  $\mathbf{G}$  are determined based on moments of the distribution function, given as follows:

$$\begin{aligned} \sum_i f_i^{\text{eq}} &= \rho, \\ \sum_i f_i^{\text{eq}} e_{i\alpha} &= \rho v_\alpha, \\ \sum_i f_i^{\text{eq}} e_{i\alpha} e_{i\beta} &= \rho c_s^2 + \sigma_{\alpha\beta} + \rho v_\alpha v_\beta, \\ \sum_i f_i^{\text{eq}} e_{i\alpha} e_{i\beta} e_{i\gamma} &\text{ should be isotropic,} \end{aligned} \quad (\text{B5})$$

where  $c_s$  is the speed of sound and is equal to  $1/\sqrt{3}$  in this model. The tensor  $\sigma_{\alpha\beta}$  represents the nonideal part of the stress tensor in the momentum balance equation. Here,  $\partial_\alpha \sigma_{\alpha\beta} = (\partial_\alpha \psi) \frac{\delta F}{\delta \psi}$ ; see Eq. (A12). While discretizing velocity space we need to ensure that the correct hydrodynamics (mass and momentum balance equations) is recovered in the continuum limit. We have used the two dimensional nine velocity (one zero velocity, four along coordinate axes, and four along lines at  $45^\circ$  to the axes, as shown in Fig. 29) lattice Boltzmann model (*D2Q9*) for current simulations. The Chapman-Enskog expansion for this model shows that proper

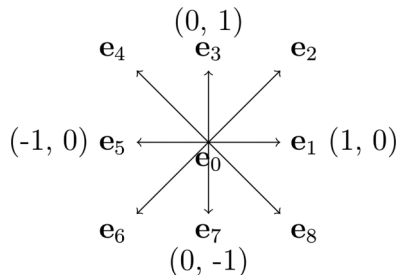


FIG. 29. Lattice velocities for *D2Q9* model.

equations describing the hydrodynamics are indeed retrieved for macroscopic systems and the kinematic viscosity  $\nu$  is given as [31]

$$\nu = (\tau_f - 0.5)c_s^2. \quad (\text{B6})$$

For viscosity contrast studies, as viscosity depends upon the relaxation time parameter [Eq. (B6)],  $\tau_f$  is assumed to be a linear function of concentration and has been varied locally using the following expression:

$$\tau_f(\mathbf{x}) = \tau_f^{(0)}(1 + \tau_f^{(1)} \times \psi(\mathbf{x})). \quad (\text{B7})$$

And since the relaxation time parameter in lattice Boltzmann simulations cannot be less than or equal to 0.5, the values of  $\tau_f^{(0)}$  and  $\tau_f^{(1)}$  are chosen such that  $\tau_f$  is always greater than 0.5. The parameter  $\tau_f^{(0)}$  is set to a rather large value of 8 in simulations and  $\tau_f^{(1)}$  is set to 0.3 and 0.5 respectively. At very high viscosity contrast, a cutoff of 0.53 is used for  $\tau_f(\mathbf{x})$  as the relaxation parameter cannot be less than 0.5 in lattice Boltzmann simulations. When the two components are assumed to have the same viscosity, the parameter  $\tau_f^{(1)}$  is set to zero, and the strain rate is a constant for an aligned system. The average viscosity ( $\bar{\mu}$ ), which is ratio of average shear stress and average strain rate, would be equal to the bare fluid viscosity [=2.5, from Eq. (B6) for the chosen values of parameters]. The relative change in viscosity ( $\Delta\mu/\bar{\mu}$ ) in this case is 0.

For systems with viscosity contrast, the velocity profile is not linear hence the strain rate depends upon the location. Here, the average strain rate ( $\bar{\gamma}$ ) is calculated by taking into account the velocity variation across one layer. This could be done as follows:

$$\begin{aligned} \bar{\gamma} &= \frac{\Delta u_x}{\lambda}, \\ &= \frac{1}{\lambda} \int_\lambda dy \dot{\gamma}, \\ &= \frac{1}{\lambda} \int_\lambda dy \frac{\sigma}{\mu'}, \end{aligned} \quad (\text{B8})$$

where  $\lambda$  is the layer width and  $\sigma$  is the shear stress. The stress here includes both Newtonian as well as the additional concentration field dependant stress. During simulations of systems with viscosity contrast, we have set the value of parameter  $r$  to 1. This corresponds to a sinusoidal concentration profile at equilibrium (see Fig. 28). Hence from Eqs. (B6) and (B7),  $\mu' = \rho[\tau_f^{(0)}(1 + \tau_f^{(1)} \times \sin(\frac{2\pi y}{\lambda})) - 0.5]c_s^2$ . The average viscosity is then calculated as

$$\bar{\mu} = \frac{\text{average stress}}{\text{average strain}} = \frac{1}{\frac{1}{\lambda} \int_\lambda \frac{dy}{\rho[\tau_f^{(0)}(1 + \tau_f^{(1)} \times \sin(\frac{2\pi y}{\lambda})) - 0.5]c_s^2}}. \quad (\text{B9})$$

The stress terms cancel out because in absence of any external body force, the stress would be constant. With  $|\psi|_{\text{max}} = 1.2$  (the observed value in simulations of initially disordered lamellar phase systems), the relative change in viscosity ( $\Delta\mu/\bar{\mu}$ ), for  $\tau_f^{(1)} = 0.3$  and  $\tau_f^{(1)} = 0.5$ , is 0.81 and 1.51 respectively. The average viscosity in these two cases is 2.37 and 2.11 respectively. The simulation results shown here are for these two values of ( $\Delta\mu/\bar{\mu}$ ).

A similar  $D2Q9$  lattice model has been used to solve convection-diffusion equation [Eq. (A10)]. A distribution function  $g_i$  is defined so that

$$\begin{aligned} \sum_i g_i &= \psi, \\ \sum_i g_i e_{i\alpha} &= \psi v_\alpha. \end{aligned} \quad (\text{B10})$$

The distribution  $g_i$  has a similar dynamical evolution equation, i.e.,

$$g_i(\mathbf{x} + \mathbf{e}_i, t + 1) - g_i(\mathbf{x}, t) = -\frac{g_i - g_i^{\text{eq}}}{\tau_g}, \quad (\text{B11})$$

where  $\tau_g$  is the relaxation time parameter for the concentration ( $\psi$ ) field. The equilibrium distribution function  $g_i^{\text{eq}}$  is assumed to be of the following form:

$$g_i^{\text{eq}}(\mathbf{x}, \mathbf{v}) = \psi [B_1^i + B_2^i(\mathbf{v} \cdot \mathbf{e}_i) + B_3^i(\mathbf{v} \cdot \mathbf{e}_i)^2 + B_4^i(\mathbf{v} \cdot \mathbf{v})]. \quad (\text{B12})$$

The coefficients ( $B_1^i - B_4^i$ ) are determined subject to the following constrains:

$$\begin{aligned} \sum_i g_i^{\text{eq}} &= \psi, \\ \sum_i g_i^{\text{eq}} e_{i\alpha} &= \psi v_\alpha, \\ \sum_i g_i^{\text{eq}} e_{i\alpha} e_{i\beta} &= \Gamma \Delta\mu \delta_{\alpha\beta} + \psi v_\alpha v_\beta, \\ \sum_i g_i^{\text{eq}} e_{i\alpha} e_{i\beta} e_{i\gamma} &\text{ should be isotropic,} \end{aligned} \quad (\text{B13})$$

where  $\Delta\mu$  is the chemical potential difference between the two components and is given as  $\Delta\mu = \frac{\delta F}{\delta \psi}$ . This choice of moments guarantees that the dynamics would be governed by the convection-diffusion equation at the continuum level [8,11] with  $\Gamma = (\tau_g - 0.5)$ .

### 1. Boundary conditions

We have used the periodic boundary condition along the flow direction and the system is sheared using either the wall boundary condition or the Lees-Edwards boundary condition.

#### a. Wall boundary condition

In lattice Boltzmann simulations, the bounce back (reflection) scheme is used to emulate a stationary surface such that

$$f_i(\mathbf{x}, t + 1) = f_{-i}(\mathbf{x}, t_+), \quad (\text{B14})$$

where the “+” sign indicates the value of the distribution function at  $(\mathbf{x}, \mathbf{e}_i)$  after collision, and  $\mathbf{e}_i = -\mathbf{e}_{-i}$ . In the case of wall driven flow, Eq. (B14) has an additional contribution proportional to wall velocity ( $\mathbf{v}_w$ ), which arises due to the Galilean invariance requirement [27]. The equation then reads [25]

$$f_i(\mathbf{x}, t + 1) = f_{-i}(\mathbf{x}, t_+) + 2A_2^i \rho \mathbf{v}_w \cdot \mathbf{e}_i. \quad (\text{B15})$$

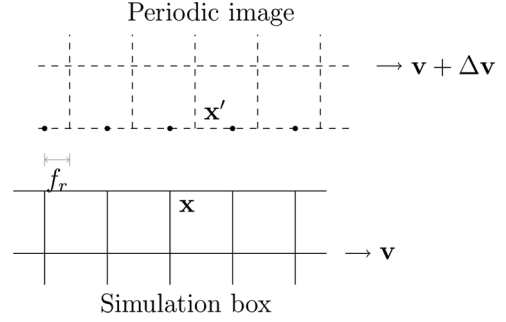


FIG. 30. Lees-Edwards boundary condition configuration. The black dots in periodic images indicate locations of  $\mathbf{x}'$  when  $f_r = 0$  (no lattice mismatch).

#### b. Lees-Edwards boundary condition

In molecular dynamics simulations, the Lees-Edwards boundary condition offers a convenient way to analyze the bulk behavior of a system under uniform shear flow by reducing the finite size effects [32]. It can be thought of as an extension of periodic boundary condition in the cross-flow direction. For 2D systems, if a particle at  $(x, y)$  with velocity  $\mathbf{v}$  leaves the system, another particle, from one of the neighboring mirror images of the system, appears in the system at location  $[x + (\Delta v_x t \bmod L_x), (y \bmod L_y)]$  with velocity  $(\mathbf{v} + \Delta\mathbf{v})$ . The implementation of the Lees-Edwards boundary condition for lattice based simulation methods involves calculating incoming distribution functions at the boundary nodes, via interpolation of distribution function densities leaving the periodic image moving with velocity  $(\mathbf{v} \pm \Delta\mathbf{v})$  above or below the simulation box. Interpolation is required due to lattice mismatch between the simulation box and the periodic image as each moves with different velocity (see Fig. 30). Based on density and velocity values over the course of the simulations, linear interpolation was found to work fairly accurately. The interpolation scheme, for the choice of lattice velocities (Fig. 29), is given as

$$\begin{aligned} f_i(x, y=0, t+1) &= (1 - f_r) f'_i(x' - e_{ix}, y=L, t_+) \\ &+ f_r f'_i(x' - e_{ix} + e_{iy}, y=L, t_+), \end{aligned} \quad (\text{B16})$$

where  $f_r = [(|\Delta v_x|t) \bmod 1]$ , and  $x' = x + (|\Delta v_x|t) - f_r$ , the largest integer smaller than  $[x + (|\Delta v_x|t)]$ . The distribution function  $f'_i(\mathbf{x}, t_+)$  is the postcollisional density at  $(\mathbf{x}, \mathbf{e}_i)$  in the periodic image and is given as [27]

$$f'_i(\mathbf{x}, t_+) = f_i(\mathbf{x}, t_+) + f_i^{\text{eq}}(\mathbf{x}, \mathbf{v} + \Delta\mathbf{v}) - f_i^{\text{eq}}(\mathbf{x}, \mathbf{v}). \quad (\text{B17})$$

The results obtained using the two boundary conditions are plotted and compared in Fig. 31. While there are quantitative differences in the results of the two boundary conditions, these differences emerge only in the long time limit after a few hundreds of strain units. The qualitative variation of both the structural properties and the viscosity with the Schmidt number (as shown in Fig. 31) as well as the other dimensionless parameters do not depend on the type of boundary conditions used.

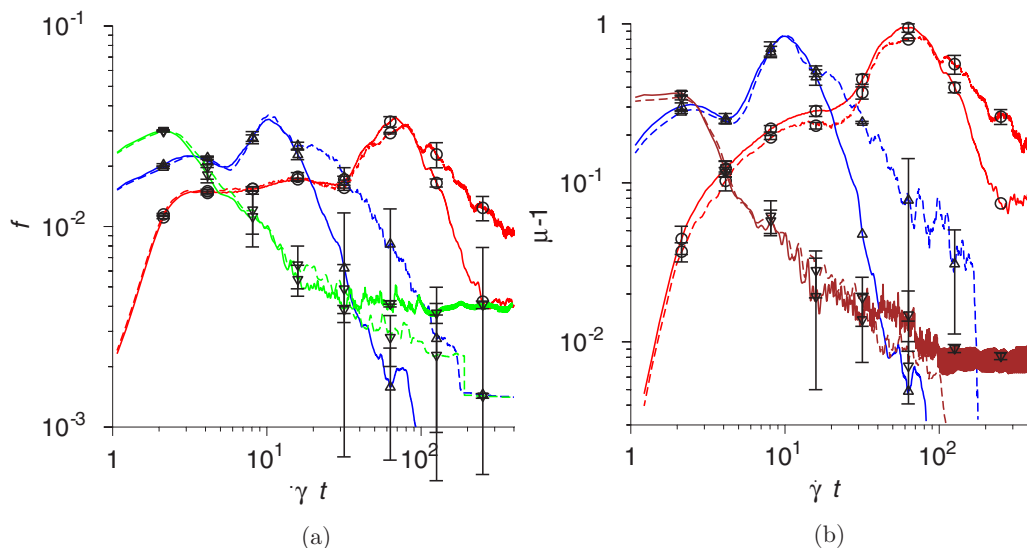


FIG. 31. Variation of the parameters  $f$  (a) and  $(\mu - 1)$  (b) with time for a lamellar system with  $Er_0 = 8 \times 10^3$ ,  $\mu_r = 0$ , and  $r = 1$  for wall (dashed lines) and Lees-Edwards periodic boundary conditions (solid lines), for Schmidt numbers 0.33 (red,  $\circ$ ), 1 (blue,  $\Delta$ ), and 5 (brown,  $\nabla$ ).

- [1] C. Meyer, S. Asnacois, C. Bourgaux, and M. Kleman, Effects of shear on a lyotropic lamellar phase, *Mol. Cryst. Liq. Cryst.* **332**, 531 (1999).
- [2] C. Meyer, S. Asnacois, and M. Kleman, Universal properties of lamellar systems under weak shear, *Eur. Phys. J. E* **6**, 245 (2001).
- [3] C.-Y. D. Lu, P. Chen, Y. Ishii, S. Komura, and T. Kato, Non-linear rheology of lamellar liquid crystals, *Eur. Phys. J. E* **25**, 91 (2008).
- [4] A. J. Bray, Theory of phase ordering kinetics, *Adv. Phys.* **43**, 357 (1994).
- [5] C. D. Yoo and J. Vinals, Anisotropic linear response in block copolymer lamellar phases, *Macromolecules* **48**, 4848 (2012).
- [6] C. D. Yoo and J. Vinals, The role of viscoelastic contrast in orientation selection of block copolymer lamellar phases under oscillatory shear, *Soft Matter* **9**, 7817 (2013).
- [7] P. C. Hohenberg and B. I. Halperin, Theory of dynamic critical phenomena, *Rev. Mod. Phys.* **49**, 435 (1977).
- [8] E. Orlandini, M. R. Swift, and J. M. Yeomans, A lattice boltzmann model of binary-fluid mixtures, *Europhys. Lett.* **32**, 463 (1995).
- [9] G. Gonnella, E. Orlandini, and J. M. Yeomans, Spinodal Decomposition to a Lamellar Phase: Effects of Hydrodynamic Flow, *Phys. Rev. Lett.* **78**, 1695 (1998).
- [10] G. Gonnella, E. Orlandini, and J. M. Yeomans, Lattice boltzmann simulations of lamellar and droplet phases, *Phys. Rev. E* **58**, 480 (1998).
- [11] V. Kumaran, S. K. Jariwala, and S. Hussain, Rheology of a lamellar liquid crystalline phase using the lattice boltzmann simulation technique, *Chem. Eng. Sci.* **56**, 5663 (2001).
- [12] A. Xu, G. Gonnella, and A. Lamura, Morphologies and flow patterns in quenching of lamellar systems with shear, *Phys. Rev. E* **74**, 011505 (2006).
- [13] V. Kumaran and D. S. S. Raman, Shear alignment of a disordered lamellar mesophase, *Phys. Rev. E* **83**, 031501 (2011).
- [14] O. Henrich, K. Stratford, D. Marenduzzo, P. V. Coveney, and M. E. Cates, Rheology of lamellar liquid crystals in two and three dimensions: a simulation study, *Soft Matter* **8**, 3817 (2012).
- [15] L. Angheluta, P. Jeraldo, and N. Goldenfeld, Anisotropic velocity statistics of topological defects under shear flow, *Phys. Rev. E* **85**, 011153 (2012).
- [16] G. Basappa, Suneel, V. Kumaran, P. R. Nott, S. Ramaswamy, V. M. Naik, and D. Rout, Structure and rheology of the defect-gel states of pure and particle-dispersed lyotropic lamellar phases, *Eur. Phys. J. B* **12**, 269 (1999).
- [17] O. Diat and D. Roux, Preparation of monodisperse multilayer vesicles of controlled size and high encapsulation ratio, *J. Phys. II France* **3**, 9 (1993).
- [18] L. Courbin, J. P. Delville, J. Rouch, and P. Panizza, Instability of a Lamellar Phase Under Shear Flow: Formation of Multilamellar Vesicles, *Phys. Rev. Lett.* **89**, 148305 (2002).
- [19] M. Kleman, *Points, Lines and Walls in Liquid Crystals, Magnetic Systems and Various Ordered Media* (John Wiley & Sons, New York, 1983).
- [20] Y. H. Kim, D. K. Yoon, H. S. Jeong, O. D. Lavrentovich, and H.-T. Jung, Smectic liquid crystal defects for self-assembling of building blocks and their lithographic applications, *Adv. Funct. Mater.* **21**, 610 (2011).
- [21] D. Boyer and J. Vinals, Grain boundary motion in layered phases, *Phys. Rev. E* **63**, 061704 (2001).
- [22] V. Kumaran, Y. K. V. V. N. Krishna Babu, and J. Sivaramakrishna, Multiscale modeling of lamellar mesophases, *J. Chem. Phys.* **130**, 114907 (2009).
- [23] V. Kumaran, Mesoscale description of an asymmetric lamellar phase, *J. Chem. Phys.* **130**, 224905 (2009).
- [24] V. Kumaran, Dynamics of edge dislocations in a sheared lamellar mesophase, *J. Chem. Phys.* **139**, 134907 (2013).
- [25] A. J. C. Ladd, Numerical simulations of particulate suspensions via a discretized boltzmann equation. part 1. theoretical foundation, *J. Fluid Mech.* **271**, 285 (1994).

- [26] A. J. Wagner and J. M. Yeomans, Phase separation under shear in two-dimensional binary fluids, *Phys. Rev. E* **59**, 4366 (1999).
- [27] A. J. Wagner and I. Pagonabarraga, Leesedwards boundary conditions for lattice boltzmann, *J. Stat. Phys.* **107**, 521 (2002).
- [28] P. Chen, Shear alignments in three-dimensional simulations of lamellar phases, *Phys. Rev. E* **71**, 061503 (2005).
- [29] S. Chapman and T. G. Cowling, *The Mathematical Theory of Non-uniform Gases* (Cambridge University Press, Cambridge, England, 1970).
- [30] P. Bhatnagar, E. P. Gross, and M. K. Krook, A model for collision processes in gases. I. small amplitude processes in charged and neutral one-component systems, *Phys. Rev.* **94**, 511 (1954).
- [31] D. A. Wolf-Gladrow, *Lattice-Gas Cellular Automata and Lattice Boltzmann Models - An Introduction* (Springer, New York, 2005).
- [32] A. W. Lees and S. F. Edwards, The computer study of transport processes under extreme conditions, *J. Phys. C: Solid State Phys.* **5**, 1921 (1972).